

Role of Convection–circulation Coupling in the Propagation Mechanism of the Madden–Julian Oscillation over the Maritime Continent in Climate Models

Yi-Chi Wang

Academia Sinica

Wan-Ling Tseng (✉ wtseng@gate.sinica.edu.tw)

Academia Sinica <https://orcid.org/0000-0002-6644-9965>

Huang-Hsiung Hsu

Academia Sinica

Research Article

Keywords: MJO, Convection Scheme, Low-Level Moistening, Climate Models

Posted Date: March 25th, 2021

DOI: <https://doi.org/10.21203/rs.3.rs-343249/v1>

License: © ⓘ This work is licensed under a Creative Commons Attribution 4.0 International License.

[Read Full License](#)

1 **Role of convection–circulation coupling in the propagation mechanism**
2 **of the Madden–Julian Oscillation over the Maritime Continent in**
3 **climate models**

4 Yi-Chi Wang¹, Wan-Ling Tseng^{1*}, Huang-Hsiung Hsu¹

5 ¹Research Center for Environmental Changes, Academia Sinica, Taipei, Taiwan

6 Corresponding author: Wan-Ling Tseng (wtseng@gate.sinica.edu.tw)

7

8 **Abstract**

9 **This study investigates the role of convection–circulation coupling on the simulated**
10 **eastward propagation of the Madden–Julian Oscillation (MJO) over the Maritime**
11 **Continent (MC). Experiments are conducted with the European Centre Hamburg**
12 **Model Version 5 (ECHAM5) coupled with the one-column ocean model – Snow-Ice-**
13 **Thermocline (SIT) and two different cumulus schemes, Nordeng (E5SIT-Nord) and**
14 **Tiedtke (E5SIT-Tied). During the early phase of MJO composites, the E5SIT-Nord**
15 **simulation reveals stronger intraseasonal anomalies in the apparent heat source (Q_1)**
16 **over the convective center, however, the E5SIT-Tied produces a stronger**
17 **background Q_1 , suggesting that deep convection prevails over the MC but does not**
18 **couple with the MJO circulation. Similarly, in the E5SIT-Tied simulation, in-**
19 **column moisture is kept mostly by local deep convection over the MC, which is in**
20 **contrast to the well-correlated relationship between moisture anomaly and MJO**
21 **circulation in E5SIT-Nord. A case study based on an observational MJO reveals**
22 **similar biases concerning of convection–circulation coupling emerges within a few**

23 **days of simulations. The E5SIT-Tied simulation produces weaker heating at the**
24 **convective center of the MJO than the E5SIT-Nord a few days after model initiation,**
25 **resulting weaker subsidence to the east and less favorable for propagation. The**
26 **present findings highlight the instantaneous responses of cumulus parameterization**
27 **schemes to MJO-related environmental changes can further affect intraseasonal**
28 **variability through altering convection–circulation coupling over the MC. Physical**
29 **schemes of moist convection are essential to realistically represent this coupling and**
30 **thereby improve the simulation of the eastward propagation of the MJO.**

31

32 **Keywords:** MJO, Convection Scheme, Low-Level Moistening, Climate Models

33

34 **1 Introduction**

35 The Madden–Julian Oscillation (MJO) is the dominant pattern of atmospheric
36 intraseasonal variability in the tropics (Madden and Julian 1972; Zhang 2005; Jiang et al.
37 2019). Numerous observational and modeling studies have explored the fundamental
38 physics regarding the eastward propagation and development of the MJO, including the
39 interaction with the frictional boundary layer (Wang and Rui 1990; Hendon and Salby
40 1994; Maloney and Hartmann 1998; Hsu et al. 2004; Kang et al. 2013), convective
41 intraseasonal air–sea interactions (Flatau, 1997; Waliser et al. 1999), ocean surface flux
42 (Maloney and Sobel 2004; Maloney 2009; Kiranmayi and Maloney 2011; Andersen and
43 Kuang 2012), moisture transport by cumulus (Benedict et al. 2007; Jiang et al. 2016,
44 2017), and air–sea interaction (DeMott et al., 2015, 2019). Despite the considerable
45 progress in state-of-the-art general circulation models (GCMs) in recent decades, realistic
46 simulations of the MJO remain difficult.

47 One challenge to improving models is the MJO is organized by strong coupling
48 between MJO circulations, convection, and ocean thermodynamics. Studies have
49 addressed numerous crucial physical processes for reproducing the MJO in GCMs,
50 including the mean state (Kim et al. 2011; Kim et al. 2017; Jiang et al. 2018; Klingaman
51 et al. 2020), convection simulated by cumulus parameterization schemes (CPS; Liu et al.
52 2005; Deng and Wu 2010; Zhou et al. 2012), convectively coupled tropical waves
53 (Kiladis et al. 2005; Janiga et al. 2018), ocean–atmosphere interaction (Tseng et al. 2015;
54 DeMott et al. 2015, 2019), the diurnal cycle of sea surface temperature (SST; Bernie et
55 al. 2005; Klingaman et al. 2011), and cloud radiative feedback (Ciesielski et al. 2017; Del

56 Genio and Chen 2015; Jiang et al. 2011). These findings jointly reflect the complexity of
57 the physical processes involved in understanding and simulating the MJO.

58 To untangle this multifaceted problem, all coupling mechanisms must be carefully
59 examined. One key aspect of the MJO behavior manifested of such coupling is MJO's
60 eastward propagation from the Indian Ocean to the Maritime Continent (MC) and onward
61 to the western Pacific (Zhang 2005). The eastward propagation of the MJO over the MC
62 has been challenging to simulate in GCMs (Zhang 2005) and remains so in the Coupled
63 Model Intercomparison Project Phase 6 models (CMIP6; Ahn et al. 2020). After the MJO
64 appears over the Indian Ocean, deep convection in the oscillation induces the dynamic
65 processes associated with the equatorial wavelike perturbations to the east over the MC,
66 further enhancing both low-level moisture convergence and moistening (Zhang 2005;
67 Jiang et al. 2020). Observational studies have suggested that the shallow convection with
68 bottom-heavy heating profiles that occurs before the propagation of the MJO convective
69 center helps precondition the development of deep convection (Kemball-Cook and Weare
70 2001; Kikuchi and Takayabu 2004). Such shallow convection that is associated with low-
71 level convergence and ascending motion moistens the lower troposphere and enhances
72 coupling with intraseasonal perturbations (Lappen and Schumacher 2014; Benedict and
73 Randall 2001). In a model experiment with prescribed heating profiles, Lappen and
74 Schumacher (2014) also demonstrated the essential role of the low-level heating in the
75 development and maintenance of the MJO.

76 Multiple studies have also reported that including air–sea coupling aids MJO
77 simulation in climate models (Tseng et al. 2015; Jiang et al. 2015; DeMott et al. 2018;
78 DeMott et al. 2019; Jiang et al. 2019). Crueger et al. (2013) explored the role of CPS,

79 ocean coupling, and model resolution by evaluating the simulation of the MJO with the
80 European Centre Hamburg Model (ECHAM) Version 6 under various configurations.
81 They have found that CPS plays an essential role in simulating MJO signatures, along
82 with ocean coupling. The researchers attributed the discrepancy to differences in the
83 sensitivity of the two CPS to tropospheric moisture (Crueger et al. 2013). However, they
84 did not discuss the role of convection-circulation coupling in their analysis. By jointly
85 using the ECHAM5 and their self-developed one-column ocean model, the Snow–Ice–
86 Thermocline (SIT) model, Tseng et al. (2015) successfully simulated the eastward
87 propagation of the MJO, observing that the low-level moisture convergence prior to the
88 active MJO phase over the MC played a pivotal role in preconditioning the propagation
89 of deep convection and circulation. The warmer SST ahead of the MJO was suggested to
90 destabilize the boundary layer and enhance frictional convergence, underscoring the
91 importance of shallow moistening for the further development of the MJO. Comparing
92 between models, Jiang et al. (2015) reported that the ECHAM5-SIT model was one of
93 the best GCMs in MJO simulations. In another study, that model was used to determine
94 the role of air–sea coupling in MJO simulations (DeMott et al. 2019). Although both
95 studies have evaluated the performance of the model in simulating the MJO, the
96 contribution of convection has not been addressed. Thus, the key mechanism underlying
97 convection–circulation coupling, which may improve MJO simulations, remains unclear.

98 To examine the role of convection in the mechanism of MJO propagation over the
99 MC with better representation of air–sea coupling, the model setup described by Tseng et
100 al. (2015) is used to analyze the convection–circulation coupling in the ECHAM5 model
101 experiments with two CPSs, namely the Nordeng scheme (E5SIT-Nord) and the Tiedtke
102 scheme (E5SIT-Tied). The same setup for modeling ocean coupling of SIT was used.

103 Using the model setup for better air–sea coupling as the basis, we investigated the role of
104 convection–circulation coupling played in the key mechanisms for better simulating the
105 eastward propagation of MJO in GCMs with CPS. In this study, we adopted the budget
106 analysis of apparent heat sources (Q_1) and apparent moisture sinks (Q_2), as well as the
107 moist static energy (MSE) budget, to the 25-year climate simulations of two model setup,
108 with the central aim of identifying the contribution of the moisture buildup over the MC
109 in the propagation of the MJO. To further clarify the effects of the representation of CPS
110 on MJO propagation, we conduct a case study by using the initial conditions from the
111 ERA-Interim reanalysis and examining the MJO evolution simulated by the two CPSs.
112 By observing how the model biases evolve in case study provides more information about
113 how biases in climate runs may link to the fast physics from CPS related to convection–
114 circulation coupling. The remainder of this paper is organized as follows. The data, model,
115 and methodology are described in Section 2. Sections 3 and 4 present the analytical results
116 and the results from the case study, respectively. The discussion and conclusion are in
117 Sections 5 and 6, respectively.

118 **2 Data, models, and methodology**

119 In the present study, the ECHAM5 (Roeckner et al. 1989) is used in combination
120 with the SIT (Tu and Tsuang 2005; Tsuang et al. 2009). As its name implies, the
121 ECHAM5 is the fifth version of the ECHAM, a GCM developed at the Max Planck
122 Institute for Meteorology. The horizontal resolution used is T63 ($\sim 1.8^\circ$), with 31 vertical
123 layers and a model top at 10 hPa (approximately 30 km). SIT simulates the SSTs and
124 variability in upper ocean temperature, including that attributable to the cool-skin and
125 diurnal warm-layer effects in the upper ocean. The turbulent kinetic energy (Gaspar et al.

126 (1990) of a water column is also simulated. In our experiments, SIT has 42 vertical layers,
127 12 of which are in the upper 10 m. In one study (Tu and Tsuang 2005), the SIT, with a 1-
128 m resolution in the upper 10 m and a layer at 0.05 mm for reproducing the cool-skin
129 effects at the ocean surface, realistically simulated the near-surface warm layer(Tu and
130 Tsuang 2005). It is not conventional to combine such a high-vertical-resolution ocean
131 model of turbulent kinetic energy to an atmospheric GCM (AGCM). To account for
132 horizontal processes, the ocean model is weakly nudged (with a 30-day time scale) to the
133 observed climatological ocean temperature at depths exceeding 10 m. The SIT and
134 ECHAM exchange SST and surface fluxes at every time step (12 min) in the tropics (30°
135 S–30° N). Elsewhere, climatological SST drives the AGCM.

136 Two CPS used in the present study are the Nordeng scheme, the default scheme used
137 in the ECHAM5 (Nordeng 1994), and the Tiedtke scheme (Tiedtke 1989). The Nordeng
138 scheme, an improved version of the Tiedtke mass flux convection scheme, considers
139 organized entrainment and detrainment in buoyancy-related penetrative convection
140 (Nordeng 1994). The differences between the two schemes lie mainly in the
141 representation of deep convection regimes, particularly closures and entrainment rates
142 (Möbis and Stevens 2012). For closures, the Tiedtke scheme uses the moisture
143 convergence within the subcloud layer to make approximation for convective intensity
144 (Tiedtke 1989). By contrast, the Nordeng scheme uses the quasi-equilibrium closure for
145 the relaxation of the vertically integrated buoyancy (Nordeng 1994). For the entrainment
146 rate, the Nordeng scheme uses additional lateral mixing; specifically, the buoyancy-
147 driven entrainment for deep convection is included in the organized entrainment module
148 (Nordeng 1994).

149 In the present study, the simulation results are analyzed using data from the Global
 150 Precipitation Climatology Project (Adler et al. 2003), data on outgoing longwave
 151 radiation and daily SST from the National Oceanic and Atmosphere Administration
 152 (Banzon et al. 2014), and atmospheric states from the ERA-Interim reanalysis (Dee et al.
 153 2011). The simulation diagnostics package developed by the Climate Variability and
 154 Predictability MJO Working Group (CLIVAR Madden–Julian Oscillation Working
 155 Group 2009) and a 20-to-100-day filter are used to isolate and determine intraseasonal
 156 variability. The MJO phases are classified on the basis of the MJO index—that is, the
 157 leading pair of principal components from an empirical orthogonal function analysis of
 158 intraseasonal outgoing longwave radiation, under zonal winds of 850 and 200 hPa
 159 (Wheeler and Hendon 2004). Because of the strong eastward propagation tendency of the
 160 MJO, the analysis is centered on the boreal cool season (November to April). The total
 161 simulation length of each experiment is 25 years, with data in the last 24 years subjected
 162 to analysis.

163 To understand the simulated convection, we calculate the Q_1 and Q_2 associated with
 164 the MJO (Yanai et al. 1973), which are presented in the following equations:

$$165 \quad Q_1 \equiv \frac{\partial \bar{s}}{\partial t} + v \cdot \nabla \bar{s} + \bar{\omega} \frac{\partial \bar{s}}{\partial p} = Q_R + L_v(\bar{c} - \bar{e}) - \frac{\partial}{\partial p} \overline{s' \omega'}$$

$$166 \quad Q_2 \equiv -L_v \left(\frac{\partial \bar{q}}{\partial t} + v \cdot \nabla \bar{q} + \bar{\omega} \frac{\partial \bar{q}}{\partial p} \right) = L_v(\bar{c} - \bar{e}) + L_v \frac{\partial}{\partial p} \overline{q' \omega'}$$

167 where c and e represent condensation and evaporation, respectively; q is the water vapor
 168 mixing ratio; s is the dry static energy ($s = cpT + gz$); and L_v is the latent heat of
 169 vaporization. As for $\overline{(\cdot)}$, it denotes the grid scale quantity relative to the subgrid
 170 components. For the convection-dominated regions, convective activities could be
 171 inferred by comparing the Q_1 and Q_2 vertical profiles to reflect the vertical transport of

172 the MSE by convection. For example, deep convection regimes often have top-heavy Q_1
 173 vertical profiles with peaks at approximately 300 hPa and Q_2 profiles with peaks at 700
 174 hPa, indicative of upward convective transport from the lower troposphere (Yanai et al.
 175 1973). By contrast, Q_1 vertical profiles in shallow convection regimes tend to be bottom-
 176 heavy, with peaks at lower atmospheric pressures (Nitta and Esbensen 1974).

177 The vertically integrated MSE budget is defined as follows:

$$178 \quad \left\langle \frac{\partial h}{\partial t} \right\rangle' = - \left\langle u \frac{\partial h}{\partial x} \right\rangle' - \left\langle v \frac{\partial h}{\partial y} \right\rangle' - \left\langle \omega \frac{\partial h}{\partial p} \right\rangle' + \langle LW \rangle' + \langle SW \rangle' + \langle LHF \rangle' + \langle SHF \rangle'$$

179 where h is the MSE ($h = cpT + gz + Lq$); u and v are the zonal and meridional velocities,
 180 respectively; ω is the vertical pressure velocity; LW and SW are the longwave and
 181 shortwave radiation fluxes, respectively; and LHF and SHF are the latent and sensible
 182 surface heat fluxes, respectively. The mass-weighted vertical integration from the surface
 183 to 200 hPa is denoted by $\langle \cdot \rangle$, and intraseasonal anomalies are represented by $\langle \cdot \rangle'$. All fields
 184 are isolated using a 20-to-100-day band-pass Lanczos filter (Duchon 1979).

185 **3 ECHAM-SIT simulations of the MJO**

186 The simulations of the MJO in two experiments involving the E5SIT-Nord and
 187 E5SIT-Tied are examined in this section. Figure 1 (a–c) presents the wavenumber–
 188 frequency spectra of simulated 850-hPa zonal winds. The E5SIT-Nord realistically
 189 simulates the 30-to-80-day eastward-propagating signals of planetary wavenumber 1
 190 (Fig. 1b), which is consistent with the finding of Tseng et al. (2015). By contrast, the
 191 spectra of the E5SIT-Tied simulation (Fig. 1c) exhibit weaker signals over wavenumber
 192 1. The remaining parts of the figure (1d–1f) illustrate the between-simulation differences
 193 in the eastward propagation of intraseasonal fluctuations under precipitation and 10-m
 194 zonal winds. The E5SIT-Nord simulation reproduces the distinctly observed eastward

195 propagation, albeit slightly more slowly, of precipitation and surface winds (Fig. 1e),
196 whereas the E5SIT-Tied simulation presents weak intraseasonal fluctuations in
197 precipitation which is decoupled from zonal winds at the MC (i.e., 120°–150° E).
198 Therefore, our analysis focuses on the convection–circulation coupling associated with
199 MJO over the MC region.

200 The mean states of zonal winds and precipitation rate are shown in Fig. S1, and maps
201 of the ratio of the intraseasonal rainfall variability to the total rainfall variability are
202 presented in Fig. S2. In line with the results of Tseng et al. (2015), the two model
203 simulations have relatively similar mean states (Fig. S1). Both models simulate a higher
204 ratio of intraseasonal rainfall variability to total variability than was observed (shaded
205 area in Fig. S2), with the E5SIT-Nord model simulating the highest variability among the
206 three datasets. By contrast, the variability simulated by the E5SIT-Tied model is weaker
207 than what was observed. While the contribution of the mean distribution of low-level
208 moisture to MJO propagation has been emphasized in numerous studies (e.g., Jiang 2017),
209 it appears not to be a major factor in our simulations, considering, as shown in Fig. S3
210 (a–c), the dryer mean state of the E5SIT-Nord simulation (relative to the E5SIT-Tied
211 simulation), especially below 700 hPa (Fig. S3d). An examination of model pattern
212 correlations with ERA-Interim (from 1000 to 200 hPa) also reveals that both models
213 effectively simulate distributions of horizontal moisture; the coefficient of correlation in
214 the both runs exceeds 0.95 (Fig. S3e). Although the mean moisture pattern appears
215 comparable, the convective processes that result in more accurate simulation of MJO
216 propagation by the E5SIT-Nord are worthy of further exploration.

217 The evolution of essential atmospheric variables for the initiation and development
218 of convection over the MC (10° S, 120°–150° E) are plotted with respect to the MJO life

219 cycle in Fig. 2. All variables underwent 20-to-100-day band-pass filtering and are plotted
220 against the simulated MJO phases, per the procedures of Wheeler and Hendon (2004).
221 Figure 2 (a–c) shows the moisture convergence associated with the simulated MJO phases.
222 The low-level convergence over the MC is the strongest below 850 hPa in phases 1 and
223 2, and it continues shifting upward into the free troposphere starting from phase 3 (Fig.
224 2a). Both simulations capture the structure of low-level moisture convergence in the first
225 two phases, but at smaller magnitudes. As shown in Fig. 2 (b-c), the simulated moisture
226 convergence shifts to the free troposphere relatively quickly between phases 3 and 4 and
227 becomes detached from the boundary layer. Moisture convergence is stronger and extends
228 to higher levels in the E5SIT-Nord simulation than in the E5SIT-Tied simulation. The
229 associated Q_1 and Q_2 over the MC region are also observable in Fig. 2 (d–f and g–i,
230 respectively). E5SIT-Nord has a sharp contrast between convective heating and cooling
231 during the MJO life cycle that is greater in amplitude than that in the E5SIT-Tied
232 simulation and in the observation data. Consistent with the wave spectrum signals in Fig.
233 1, the magnitudes of Q_1 and Q_2 in the E5SIT-Tied simulation are substantially weaker
234 than those in the E5SIT-Nord simulation. Notably, the observed Q_2 exhibits a distinct tilt,
235 and both models simulate a rapid transition from the near-surface features to the deep
236 convective structure in the middle troposphere. Figure 2 (j–l) presents the evolution of
237 the MSE profiles over the MC associated with MJO phases. The vertical development of
238 the MSE, specifically through the upward transport of moisture from the near-surface to
239 the low-level troposphere, results in conditions conducive to deep convection (Fig. 2j).
240 The E5SIT-Nord simulates the gradual upward development of MSE with time, whereas
241 the E5SIT-Tied (Fig. 2k, l) simulates weak preconditioning with an unstable near-surface
242 layer, followed by the sudden onset of high MSE and deep convection in mature phases.

243 As noted by Tseng et al. (2015), this moistening process, characterized by the tilting of
 244 MSE, was only captured when the ECHAM5 was used in concert with the SIT.

245 As tropical convection has a multiscale nature, convective activities on other time
 246 scales can affect MJO-related convection development. Figure 3 presents the unfiltered
 247 Q_1 and Q_2 in eight MJO phases, corresponding to the intraseasonal ones shown in Fig. 2
 248 (d–i). In the reanalysis, the Q_1 and Q_2 profiles (Fig. 3a, d) reveal the evolution of the
 249 convective activities in the MJO, from the shallow convection in the earlier phases to the
 250 deep convection in the mature phases. Both models simulate heating or moistening over
 251 all phases that are stronger in magnitude than their observed counterparts. In the E5SIT-
 252 Nord experiment, the simulated Q_1 exhibits heating during the mature phases that is
 253 comparable to its observed counterpart; however, in phase 4, heating is greatly
 254 overestimated by as much as 4 K/day (Fig. 3b). By contrast, in the E5SIT-Tied experiment,
 255 Q_1 heating persists from phase 3 to phase 8 (Fig. 3c). Notably, the mean Q_1 in the E5SIT-
 256 Tied simulation is larger than that in the E5SIT-Nord simulation when averaged over the
 257 entire MJO life cycle, the opposite of the Q_1 projection on the intraseasonal time scale
 258 (Fig. 2). Unlike the prominent Q_1 associated with MJO convective center in the
 259 observation data and the E5SIT-Nord simulation, the Q_1 heating in the E5SIT-Tied
 260 simulation persists from phases 1 to 8 of the MJO, demonstrating the maintenance of deep
 261 convection over the MC. This result and its relationship with lower simulation skill of
 262 MJO is explored in later sections.

263 We focus on the convection activities over the MC during phases 1 and 2 of the MJO,
 264 when the deep convection center is over the Indian Ocean. Figure 4 shows the Q_1/Q_2
 265 profiles over 10° S and 120° – 150° E during these phases in the ERA-Interim analysis, in
 266 the E5SIT-Nord simulation, and in the E5SIT-Tied simulation. In phase 1, the peak of Q_1

267 in the reanalysis exhibits relatively homogeneous heating at a maximum rate of 1 K/day,
 268 suggesting a relative clear atmosphere with radiative heating and shallow convective
 269 heating dominate Q_1 (red line in Fig. 4a). The Q_2 profile peaks at 700 hPa, indicating
 270 drying within the planetary boundary layer (PBL) and moistening in the lower
 271 troposphere. Such profiles suggest that during this period, moisture is transported from
 272 the PBL to the lower troposphere over the MC (blue line in Fig. 4a) through bottom-heavy
 273 convection. In the E5SIT-Nord, during phase 1, the Q_1 value peaks at approximately 700
 274 hPa, with a bottom-heavy profile. At the same time, the Q_1 and Q_2 peaks correspond to
 275 each other, implying that convection is shallow at this point, mainly moistening the low-
 276 level troposphere (Fig. 4b). By contrast, in the E5SIT-Tied simulation, the Q_1 and Q_2
 277 profiles peak near 500 and 700 hPa, respectively, suggesting deep, intense convection
 278 over the MC (Fig. 4c). As shown in Fig. 4 (d–f), deep convective heating at approximately
 279 500 hPa is higher in phase 2 in both the ERA-Interim analysis and the two simulations.
 280 As is the case in phase 1, heating is deeper and more intense in the E5SIT-Tied simulation
 281 than in the E5SIT-Nord simulation or the ERA-Interim reanalysis.

282 Figure 5 shows the MJO structures in phases 1 and 2, with overturning circulation
 283 indicated by vectors with Q_1 (shading) and moisture convergence (green contours). The
 284 shaded area and the contours of the horizontal maps represent the precipitation and sea
 285 level pressure, respectively (bottom panel in Fig.5). In phases 1 and 2, the MJO
 286 precipitation is concentrated over the central Indian Ocean (around 80°–90° E), with a
 287 strong upward trend. At the same time, subsidence is considerable over the MC—
 288 specifically, in a region characterized by low-level moisture convergence (around 120°–
 289 150° E; Fig. 5a). During this phase, E5SIT-Nord simulates strong subsidence and low-
 290 level moisture convergence over the MC and low-level easterlies over the eastern Indian

291 Ocean (Fig. 5b). By contrast, E5SIT-Tied simulates very weak subsidence and easterlies
 292 over the MC and the eastern Indian Ocean, respectively, indicating weak convection–
 293 circulation coupling.

294 Figure S4, which presents an analysis of the MSE budget over the MC (10° S, 120°–
 295 150° E, spanning the area from the Banda Sea to the Maluku Islands and Java) during
 296 phases 1 and 2, elucidates the differences between the two simulations and the ERA-
 297 Interim reanalysis. Among the budget terms in E5SIT-Nord, those concerning horizontal
 298 and vertical advection terms contribute positively to the tendency term, which is partially
 299 cancelled out by longwave radiation. By contrast, the E5SIT-Tied simulates less vertical
 300 advection and very weak negative horizontal advection. The cancellation by longwave
 301 radiation results in an almost negligible tendency. The principal differences between the
 302 E5SIT-Nord and E5SIT-Tied simulations appears to be in the horizontal advection term
 303 and vertical advection terms, which further result in the poorer ability of E5SIT-Tied to
 304 simulate the propagation of the MJO. In phase 2, differences in horizontal advection that
 305 become the dominant term in the MSE budget increase as convection moves closer to the
 306 MC (Fig. S4b). Although the budget terms computed from the reanalysis have large MSE
 307 residuals, as in previous studies (Kiranmayi and Maloney 2011; Jiang 2017), vertical and
 308 horizontal advection likely to be crucial contributors to MSE tendency; this is highly
 309 consistent with that calculated from the E5SIT-Nord simulation.

310 To further visualize the coupling of moisture buildup and the MJO over the MC, we
 311 examine the large-scale circulation patterns and thermodynamics during periods when the
 312 moisture buildup over the MC is the most substantial. We first define intraseasonal
 313 moisture buildup by characterizing the duration of moisture residence in the tropospheric
 314 column before removal through rain ($[\int_{p_B}^{p_T} q dp]/[P]$) over the southern MC (10° S–10° N,

315 120° – 150° E), where $[\cdot]$ is the intraseasonal filtering, q is moisture, P is the rain rate, p_T
 316 is the pressure at the cloud top, and p_B is the pressure at the cloud bottom. The normalized
 317 convective time scale over the southern MC are calculated with respect to the lag-
 318 regressed fields to RMM1 index with ERA-Interim and two model runs in Figure S5. In
 319 ERA-Interim, convective time scale over the MC increases gradually from phase 1 (i.e.,
 320 -20 days), reaching the maximum in phase 2 (i.e., -12 days; green line in Fig. S5),
 321 indicating moisture buildup peaks around 10 days before the deep convection activity on
 322 day 0 and under dominant shallow convection (from Q_1/Q_2 in Fig. 2). Figure 6 presents
 323 the regressed structure of the Q_2 , MSE, and wind fields on the time series of accumulation
 324 (Fig. S5) in the ERA-Interim reanalysis, E5SIT-Nord simulation, and E5SIT-Tied
 325 simulation. A distinct feature of MJO with convective center at the Indian ocean and
 326 dynamical responses are shown in both the reanalysis and the E5SIT-Nord simulation.
 327 Notably, a realistic structure similar to Kelvin waves with two off-equatorial MSE
 328 maxima over the eastern Indian Ocean under strong easterlies at the equatorial MC is
 329 present only in the E5SIT-Nord simulation. On the other hand, the missing of the deep
 330 convection signal over the east Indian Ocean and west MC are shown in the E5SIT-Tied
 331 run (Fig. 6c). Also in reanalysis and E5SIT-Nord, the zonal-height cross-section exhibits
 332 a tilted structure of well-located MSE and Q_2 , which depicts a MJO structure in the
 333 developing phase (at approximately phase 2) (Fig. 6a, b). The tilted structure involves
 334 deep convection near 90° E, relatively shallow convection at 120° E, and low-level
 335 moistening by convective processes between 120° E and 150° E. The Q_2 tilt in the E5SIT-
 336 Nord is more rapid than that in the ERA-Interim reanalysis (as indicated by blue contours
 337 in the right panels of Fig. 6a, b). Such westward-tilting vertical structures have been
 338 identified in numerous observational studies (Kiladis et al. 2005; Kim et al. 2009; Tseng

339 et al. 2015; Jiang et al. 2015). By contrast, the E5SIT-Tied simulation reveals local deep
340 convection and a MSE maximum over the MC (120° – 150° E), implying the MSE
341 anomaly over MC couple only with local convection activity, not with the large-scale
342 circulation patterns that are further linked to deep convection in the Indian Ocean. The
343 meridional cross-section over 120° – 150° E also indicates the anomalies in the deep Q_2
344 and the MSE over the MC in the E5SIT-Tied simulation (Fig. S6). By contrast, both the
345 E5SIT-Nord simulation and the ERA-Interim reanalysis exhibit a shallower Q_2 and MSE
346 structure, with the maximum at approximately 800 hPa. As in the ERA-Interim reanalysis
347 and the E5SIT-Nord simulation, this is a precondition for the development of deep
348 convection over the MC and the eastward propagation of the MJO when convection is
349 still over the Indian Ocean.

350 The characteristics of convective moistening (i.e., Q_2) to rainfall categories and SST
351 are presented as follows to investigate the impacts of convective process on environments.
352 Figure 7 shows the Q_2 profiles stratified by the daily rain rate averaged over the tropical
353 oceans (10° S– 5° N, 80° – 160° E) in the two model runs and the reanalysis. For low rain
354 rates, the E5SIT-Nord simulates a more bottom-heavy Q_2 profile than the E5SIT-Tied
355 does, causing greater moistening in the PBL. For high rain rates, E5SIT-Nord accurately
356 simulates stronger drying (more latent heating) in the middle troposphere associated with
357 strong convective activity. The two characteristics (i.e., stronger low-level moistening
358 and stronger deep drying) of the E5SIT-Nord simulation help create more favorable
359 environmental conditions for the propagation of the MJO. Figure 8 shows the percentage
360 of rainfall occurrences stratified with respect to SST and rainfall intensity. The highest
361 rainfall is noted between 28° C and 30° C (Fig. 8a, b) in both the observation and the

362 E5SIT-Nord simulation. By contrast, the E5SIT-Tied simulates more frequent rainfall
363 when the SST is higher than 30°C, suggesting that the presence of convection does not
364 allow for the simulation of a proper rainfall–SST relationship. As shown in Fig. 8c, the
365 E5SIT-Tied tends to be overresponsive to high SST, producing an excessive amount of
366 local convective rainfall.

367 **4 Case study on the MJO involving two CPSs**

368 The difference in the representation of convection–circulation coupling in the two
369 simulations may not be directly ascribable to the representation of the convective
370 processes in the CPS. To examine the relationship between the instantaneous convective
371 response to the MJO circulation and convection–circulation biases found in climate runs,
372 we conduct a simulation of an MJO case, using initial conditions from the ERA-Interim
373 reanalysis. Having the setup of the two schemes, the simulation is initiated at the start
374 point of October 31, 2011, when a well-developed MJO is observed over the Indian Ocean.
375 The two experiments are then integrated for 3 days and analyzed for their differences in
376 days 1 and 2. This setup is designed to compare the response of moist convection
377 processes and ensure that the large-scale circulation patterns remain close to the initial
378 conditions. The diagnostics are useful for understanding the biases caused by the model
379 representation of convective processes from diurnal to interannual time scales (Ma et al.
380 2021).

381 Figure 9 shows the differences in circulation patterns and sea level pressure between
382 the two simulations, in the form of a height–longitude cross-section and horizontal maps,
383 on the first and second days after model initiation. On day 1, the convection center of the
384 MJO is over the tropical Indian Ocean (near 90° E), with weak subsidence in the east over

385 the MC and the western Pacific. After 1-day integration, the E5SIT-Nord simulation
386 produces (1) stronger upward motion associated with convective center at 90° E and (2)
387 a stronger basin-wide subsidence over the MC and the western Pacific from 120° E to
388 180° E (Fig. 9a). In accompany with circulations, stronger convective drying represented
389 by Q2 in E5SIT-Nord at the convective center compared with E5SIT-Tied (shown as
390 green contours in Fig.9a). To the east of deep convective center of MJO, the convection
391 over the MC in the E5SIT-Nord simulation in response to the subsidence is much
392 shallower than that in the E5SIT-Tied simulation, especially over the Borneo, near 120°
393 E (green contours in Fig.9a). Notably, in the E5SIT-Nord simulation, more moisture is
394 available in the lower troposphere and less moisture is available in the PBL below 850hPa
395 over the MC and the western Pacific (represented by MSE; shading in Fig.9a); this is
396 indicative of stronger shallow convection that helps create a favorable environment for
397 deep convection. In the meantime, the E5SIT-Nord presents a horizontal structure similar
398 to Kelvin waves which appears in the zonal dipole of sea level pressure, forming easterlies
399 over the equatorial MC and the eastern equatorial Indian Ocean (bottom panel in Fig. 9a).
400 This implies that the deep convection heating in the E5SIT-Nord simulation produces
401 stronger dynamic responses than E5SIT-Tied simulation.

402 On day 2, when the convective center moves toward the western MC, different responses
403 attributable to the two schemes become more substantial. Relative to the E5SIT-Tied
404 simulation, the stronger upward motion at the convective center of the E5SIT-Nord
405 simulation leads to stronger subsidence and enhanced tropical easterlies extending to the
406 western Pacific (arrows in the bottom panel of Fig. 9b). Notably, a more prominent
407 structure of Kelvin waves appears in response to both winds and sea level pressure (near
408 130° E, 10° N; bottom panel of Fig. 9b). In addition to the enhanced easterlies, the

409 meridional winds at the north side of the equator also become stronger, which in turn
410 enhances low-level convergence at the equator. Accompanying the vertical transport of
411 shallow convection, more moisture accumulates over the low levels between 800 and 500
412 hPa in the E5SIT-Nord simulation, providing conditions more conducive for MJO
413 propagation, as mentioned in other studies (Kiranmayi and Maloney 2011; Adames 2017;
414 Maloney et al. 2019). Consistent with the findings on climatological MJO composites in
415 Fig. 7, these features also suggest that E5SIT-Nord can simulate stronger convective
416 heating in the deep convection regime and greater moistening in the shallow convection
417 regime than the E5SIT-Tied can.

418 **5 Discussion**

419 The comparison of the two model simulations against observational data revealed
420 the importance of proper coupling between convection and large-scale circulation
421 patterns in climate models to the realistic simulation of the MJO. In the E5SIT-Tied
422 simulation, the persistent but fleeting period of deep convection dries out the moisture
423 over the MC even during MJO development, resulting in conditions that are less favorable
424 for MJO propagation. By contrast, E5SIT-Nord better simulates the moisture buildup
425 over the MC during MJO development, facilitating the propagation of the MJO over deep
426 convective regions. Figure 10 presents the differences between the model simulations
427 with regard to the convection–circulation coupling during MJO development.

428 Based on our results, we suggest two aspects of convection–circulation coupling that
429 are vital to improving simulations of MJO propagation: (1) the ability to generate deep
430 convective heating and induce subsidence to the east of convective center and (2) the
431 ability to induce moisture buildup in the subsidence region and create an environment

432 that is conducive to the later development of deep convection. During the early phases of
433 the MJO, when the convective center is located in the Indian Ocean, deep heating induces
434 Kelvin-wave-like perturbations (e.g., easterlies and low-pressure anomalies) that extend
435 eastward with a subsidence branch to the MC and the western Pacific (Milliff and Madden
436 1996; Hendon and Salby 1996; Cravatte et al. 2003; Kiladis et al. 2005). If the deep
437 convective heating is only weakly simulated, the induced subsidence becomes too weak
438 to suppress the deep convection over the MC region where the SST is high. The
439 preconditioning for the propagation of the MJO to the MC also requires the buildup of
440 low-level moisture, which is often caused by the moistening effect of shallow convection
441 (from the transport of moisture from the PBL). Such moisture buildup is often controlled
442 by the representation of moist convection in climate models, especially in the
443 determination of the type of convection and the associated heating/moistening. When the
444 convection in the model is overly sensitive to high SST, convection can be frequently
445 triggered, depleting moisture and precluding the realistic simulation of the moistening
446 process over the MC when MJO is approaching. Our analysis also suggests that climate
447 models must be capable of producing the contrast between light and intense rainfall
448 events—that is, to simulate deep heating with intense rainfall and shallow moistening
449 with light rainfall. E5SIT-Tied is more likely to present weaker and more frequent
450 convection than its observed counterpart and also lighter than that simulated by E5SIT-
451 Nord. Such a tendency results in a more stable atmosphere, which makes it more
452 challenging to model the convection–circulation coupling with MJO in E5SIT-Tied.

453 Numerous studies have indicated that the design of convection schemes is essential
454 to accurately simulating the MJO, including the sensitivity of CPS to the tropospheric
455 moisture by entrainment or detrainment (Hannah and Maloney 2014), momentum

456 transport (Wu et al. 2007; Miyakawa et al. 2012), microphysical processes, intensity
457 closure (Zhang and Mu 2005; Peters et al. 2017), triggering (Peters et al. 2017), the
458 representation of stratiform convection (Fu and Wang 2009), and shallow convection
459 (Zhang and Song 2009). The discrepancies between simulations observed in the present
460 study could be attributable to various differences in the design of the Nordeng and Tiedtke
461 schemes, such as the sensitivity to tropospheric humidity caused by entrainment design
462 (Möbis and Stevens 2012). We take a diagnostic approach, interpreting these differences
463 in a context of convection-circulation coupling. To ensure the successful simulation of
464 MJO propagation, the model representations of convection must be consistent. The
465 similarity in the biases concerning convection–circulation coupling as observed in both
466 the case study and the climate simulations suggests that biases in fast convective response
467 can further induce intraseasonal biases. To improve the simulation of intraseasonal
468 variability by better representing convection–circulation coupling, it is necessary to
469 carefully design responses of CPS to environmental characteristics, such as wind,
470 humidity, and SST. The process-based diagnostic used in the present study is useful for
471 understanding model performance with regard to convection–circulation coupling and
472 can also be used to evaluate designs of CPS for MJO simulation.

473 Although we focus on the CPS, MJO-related convection–circulation coupling
474 actually depends on the combined effects of moist convection designs, including shallow
475 convection, the PBL, and the parameterization of air–sea interaction. For example, with
476 regard to application in models derived from the Community Atmospheric Model 2, Liu
477 et al. (2005) concluded that the Tiedtke scheme outperforms the Nordeng scheme because
478 of its ability to trigger convection with low-level convergence. Considering that the
479 ECHAM5 used here had different PBL schemes and shallow convection schemes from

480 Community Atmosphere Model 2, the moisture buildup processes that are involved are
481 likely to differ substantially. The simulations in the present study considered air–sea
482 coupling, which, according to DeMott et al. (2019), are crucial contributors to the low-
483 level moistening observed in successful MJO simulations. Although it is beyond the
484 scope of this study, the short period of convection in the E5SIT-Tied simulation likely
485 allows more shortwave radiation to warm ocean regions, enhancing the SST, and further
486 destabilizes atmosphere, causing positive feedback between convection and SST. This
487 feedback strengthens the convective responses to SST and hinders the coupling of
488 convection with large-scale circulation patterns such as those in the MJO. Therefore, the
489 holistic consideration of moist convection and air–sea coupling is necessary to improve
490 the representation of the MJO in climate models. This premise warrants further
491 investigation.

492 **6 Conclusion**

493 We conducted experiments using the ECHAM model with one-column high
494 resolution ocean model to investigate the key processes for MJO propagation over the
495 MC in climate simulations. With models with better representation of air–sea coupling,
496 we demonstrated that convection–circulation coupling is crucial to the modeling of MJO
497 propagation over the MC. E5SIT-Tied simulates less moisture buildup over the MC when
498 the deep convection in phases 1 and 2 is necessary for the propagation of the MJO over
499 the MC. The E5SIT-Tied simulation, which does not model MJO propagation, produces
500 local MSE anomaly which is greatly correlated with local deep convection over the MC,
501 in contrast to the shallow convection simulated by E5SIT-Nord. Such rapid development
502 of deep convection over the MC creates an environment that is less conducive to MJO

503 propagation. Differences in low-level moistening in relation to light rain events between
504 the two simulations indicated that E5SIT-Tied tends to remove more moisture through
505 convective processes in the presence of subsidence than does E5SIT-Nord. The hindcast
506 case study of an observed MJO indicated that the environments that are less favorable for
507 the eastward propagation of the MJO in the E5SIT-Tied simulation may be formed
508 through weaker deep convective heating at the convective center of the MJO, which in
509 turn leads to weaker subsidence and moisture buildup over the MC and the western
510 Pacific. The present findings suggest that even with air–sea coupling, MJO propagation
511 over the MC is highly dependent on the capacity of CPS to produce MJO-related
512 convection-circulation coupling, including (1) inducing strong deep convective heating
513 associated with convective center over the Indian Ocean and (2) forming a favorable
514 environment characterized by low-level moistening under the effects of a subsidence
515 branch to the east of convective center. If CPSs are capable of this, convection–circulation
516 coupling is reinforced, and the maintenance of convective processes of the MJO over the
517 MC is facilitated. Our analysis indicates that the instantaneous response of CPS to MJO-
518 related environmental changes can further affect intraseasonal variability in climate
519 models; thus, the response of CPS must be carefully designed. Our analysis may be used
520 as a process-based diagnostic for evaluating convection–circulation coupling in the MJO.
521 Our findings can help model developers resolve the challenge of the “MJO barrier” over
522 the MC, helping them better forecast MJO in their climate models.

523 **Acknowledgments**

524 This work was supported by the Taiwan Ministry of Science and Technology
525 under grant numbers MOST 105-2119-M-001-018, MOST107-2111-M-001-010, MOST
526 109-2111-M-001-012-MY3, and MOST 109-2123-M-001-004. We are also grateful to

527 the National Center for High-Performance Computing for providing the facilities for the
 528 computational procedures and to the Max Planck Institute for Meteorology, which
 529 developed the ECHAM5.

530

531 **References**

- 532 Adler RF, Huffman GJ, Chang A, et al (2003) The Version-2 Global Precipitation
 533 Climatology Project (GPCP) Monthly Precipitation Analysis (1979–Present). *J*
 534 *Hydrometeorol* 4:1147–1167. [https://doi.org/10.1175/1525-](https://doi.org/10.1175/1525-7541(2003)004<1147:TVGPCP>2.0.CO;2)
 535 [7541\(2003\)004<1147:TVGPCP>2.0.CO;2](https://doi.org/10.1175/1525-7541(2003)004<1147:TVGPCP>2.0.CO;2)
- 536 Ahn M, Kim D, Kang D, et al (2020) MJO Propagation Across the Maritime Continent:
 537 Are CMIP6 Models Better Than CMIP5 Models? *Geophys Res Lett* 47:.
 538 <https://doi.org/10.1029/2020GL087250>
- 539 Banzon VF, Reynolds RW, Stokes D, Xue Y (2014) A 1/4°-Spatial-Resolution Daily
 540 Sea Surface Temperature Climatology Based on a Blended Satellite and in situ
 541 Analysis. *J Clim* 27:8221–8228. <https://doi.org/10.1175/JCLI-D-14-00293.1>
- 542 CLIVAR Madden-Julian Oscillation working group (2009) MJO Simulation
 543 Diagnostics. *J Clim* 22:3006–3030. <https://doi.org/10.1175/2008JCLI2731.1>
- 544 Cravatte S, Picaut J, Eldin G (2003) Second and first baroclinic Kelvin modes in the
 545 equatorial Pacific at intraseasonal timescales. *J Geophys Res* 108:22-1-22–20.
 546 <https://doi.org/10.1029/2002JC001511>
- 547 Crueger T, Stevens B, Brokopf R (2013) The Madden–Julian Oscillation in ECHAM6
 548 and the Introduction of an Objective MJO Metric. *J Clim* 26:3241–3257.
 549 <https://doi.org/10.1175/JCLI-D-12-00413.1>
- 550 Dee DP, Uppala SM, Simmons AJ, et al (2011) The ERA-Interim reanalysis:

- 551 configuration and performance of the data assimilation system. *Q J R Meteorol Soc*
 552 137:553–597. <https://doi.org/10.1002/qj.828>
- 553 DeMott CA, Klingaman NP, Tseng W, et al (2019) The Convection Connection: How
 554 Ocean Feedbacks Affect Tropical Mean Moisture and MJO Propagation. *J*
 555 *Geophys Res Atmos* 124:11910–11931. <https://doi.org/10.1029/2019JD031015>
- 556 Duchon CE (1979) Lanczos Filtering in One and Two Dimensions. *J Appl Meteorol*
 557 18:1016–1022. <https://doi.org/10.1175/1520->
 558 0450(1979)018<1016:LFIOAT>2.0.CO;2
- 559 Fu X, Wang B (2009) Critical Roles of the Stratiform Rainfall in Sustaining the
 560 Madden–Julian Oscillation: GCM Experiments*. *J Clim* 22:3939–3959.
 561 <https://doi.org/10.1175/2009JCLI2610.1>
- 562 Gaspar P, Grégoris Y, Lefevre J-M (1990) A simple eddy kinetic energy model for
 563 simulations of the oceanic vertical mixing: Tests at station Papa and long-term
 564 upper ocean study site. *J Geophys Res* 95:16179.
 565 <https://doi.org/10.1029/JC095iC09p16179>
- 566 Hannah WM, Maloney ED (2014) The moist static energy budget in NCAR CAM5
 567 hindcasts during DYNAMO. *J Adv Model Earth Syst* 6:420–440.
 568 <https://doi.org/10.1002/2013MS000272>
- 569 Hendon HH, Salby ML (1994) The Life Cycle of the Madden–Julian Oscillation. *J*
 570 *Atmos Sci* 51:2225–2237. <https://doi.org/10.1175/1520->
 571 0469(1994)051<2225:TLCOTM>2.0.CO;2
- 572 Hendon HH, Salby ML (1996) Planetary-Scale Circulations Forced by Intraseasonal
 573 Variations of Observed Convection. *J Atmos Sci* 53:1751–1758.
 574 [https://doi.org/10.1175/1520-0469\(1996\)053<1751:PSCFBI>2.0.CO;2](https://doi.org/10.1175/1520-0469(1996)053<1751:PSCFBI>2.0.CO;2)

- 575 Jiang X (2017) Key processes for the eastward propagation of the Madden-Julian
576 Oscillation based on multimodel simulations. *J Geophys Res Atmos* 122:755–770.
577 <https://doi.org/10.1002/2016JD025955>
- 578 Jiang X, Waliser DE, Xavier PK, et al (2015) Vertical structure and physical processes
579 of the Madden-Julian oscillation: Exploring key model physics in climate
580 simulations. *J Geophys Res Atmos* 120:4718–4748.
581 <https://doi.org/10.1002/2014JD022375>
- 582 Kiladis GN, Straub KH, Haertel PT (2005) Zonal and vertical structure of the Madden--
583 Julian oscillation. *J Atmos Sci* 62:2790–2809
- 584 Kim D, Sperber K, Stern W, et al (2009) Application of MJO Simulation Diagnostics to
585 Climate Models. *J Clim* 22:6413–6436. <https://doi.org/10.1175/2009JCLI3063.1>
- 586 Kiranmayi L, Maloney ED (2011) Intraseasonal moist static energy budget in reanalysis
587 data. *J Geophys Res Atmos* 116:
- 588 Liu P, Wang B, Sperber KR, et al (2005) MJO in the NCAR CAM2 with the Tiedtke
589 convective scheme. *J Clim* 18:3007–3020
- 590 Ma H-Y, Zhou C, Zhang Y, et al (2021) A multi-year short-range hindcast experiment
591 with CESM1 for evaluating climate model moist processes from diurnal to
592 interannual timescales. *Geosci Model Dev* 14:73–90. [https://doi.org/10.5194/gmd-](https://doi.org/10.5194/gmd-14-73-2021)
593 [14-73-2021](https://doi.org/10.5194/gmd-14-73-2021)
- 594 Madden RA, Julian PR (1972) Description of Global-Scale Circulation Cells in the
595 Tropics with a 40–50 Day Period. *J Atmos Sci* 29:1109–1123.
596 [https://doi.org/10.1175/1520-0469\(1972\)029<1109:DOGSCC>2.0.CO;2](https://doi.org/10.1175/1520-0469(1972)029<1109:DOGSCC>2.0.CO;2)
- 597 Milliff RF, Madden RA (1996) The Existence and Vertical Structure of Fast, Eastward-
598 Moving Disturbances in the Equatorial Troposphere. *J Atmos Sci* 53:586–597.

- 599 [https://doi.org/10.1175/1520-0469\(1996\)053<0586:TEAVSO>2.0.CO;2](https://doi.org/10.1175/1520-0469(1996)053<0586:TEAVSO>2.0.CO;2)
- 600 Miyakawa T, Takayabu YN, Nasuno T, et al (2012) Convective Momentum Transport
601 by Rainbands within a Madden–Julian Oscillation in a Global Nonhydrostatic
602 Model with Explicit Deep Convective Processes. Part I: Methodology and General
603 Results. *J Atmos Sci* 69:1317–1338. <https://doi.org/10.1175/JAS-D-11-024.1>
- 604 Möbis B, Stevens B (2012) Factors controlling the position of the Intertropical
605 Convergence Zone on an aquaplanet. *J Adv Model Earth Syst* 4:n/a-n/a.
606 <https://doi.org/10.1029/2012MS000199>
- 607 Nitta T, Esbensen S (1974) Heat and Moisture Budget Analyses Using BOMEX Data.
608 *Mon Weather Rev* 102:17–28. [https://doi.org/10.1175/1520-](https://doi.org/10.1175/1520-0493(1974)102<0017:HAMBAU>2.0.CO;2)
609 [0493\(1974\)102<0017:HAMBAU>2.0.CO;2](https://doi.org/10.1175/1520-0493(1974)102<0017:HAMBAU>2.0.CO;2)
- 610 Nordeng T (1994) Extended versions of the convection parametrization scheme at
611 ECMWF and their impact upon the mean climate and transient activity of the
612 model in the tropics. Res Dep Tech Memo 206:
- 613 Peters K, Crueger T, Jakob C, Möbis B (2017) Improved MJO-simulation in
614 ECHAM6.3 by coupling a Stochastic Multicloud Model to the convection scheme.
615 *J Adv Model Earth Syst* 9:193–219. <https://doi.org/10.1002/2016MS000809>
- 616 Roeckner E, Dumenil L, Kirk E, et al (1989) The Hamburg version of the ECMWF
617 model (ECHAM). Res Act Atmos Ocean Model CAS/JSC Work Gr Numer Exp
618 13:7--1
- 619 Tiedtke M (1989) A Comprehensive Mass Flux Scheme for Cumulus Parameterization
620 in Large-Scale Models. *Mon Weather Rev* 117:1779–1800.
621 [https://doi.org/10.1175/1520-0493\(1989\)117<1779:ACMFSF>2.0.CO;2](https://doi.org/10.1175/1520-0493(1989)117<1779:ACMFSF>2.0.CO;2)
- 622 Tseng W-L, Tsuang B-J, Keenlyside NS, et al (2015) Resolving the upper-ocean warm

- 623 layer improves the simulation of the Madden–Julian oscillation. *Clim Dyn*
 624 44:1487–1503. <https://doi.org/10.1007/s00382-014-2315-1>
- 625 Tsuang B-J, Tu C-Y, Tsai J-L, et al (2009) A more accurate scheme for calculating
 626 Earth’s skin temperature. *Clim Dyn* 32:251–272. [https://doi.org/10.1007/s00382-](https://doi.org/10.1007/s00382-008-0479-2)
 627 008-0479-2
- 628 Tu C-Y, Tsuang B-J (2005) Cool-skin simulation by a one-column ocean model.
 629 *Geophys Res Lett* 32:n/a-n/a. <https://doi.org/10.1029/2005GL024252>
- 630 Wang B, Rui H (1990) Dynamics of the Coupled Moist Kelvin–Rossby Wave on an
 631 Equatorial β -Plane. *J Atmos Sci* 47:397–413. [https://doi.org/10.1175/1520-](https://doi.org/10.1175/1520-0469(1990)047<0397:DOTCMK>2.0.CO;2)
 632 0469(1990)047<0397:DOTCMK>2.0.CO;2
- 633 Wheeler MC, Hendon HH (2004) An All-Season Real-Time Multivariate MJO Index:
 634 Development of an Index for Monitoring and Prediction. *Mon Weather Rev*
 635 132:1917–1932. [https://doi.org/10.1175/1520-](https://doi.org/10.1175/1520-0493(2004)132<1917:AARMMI>2.0.CO;2)
 636 0493(2004)132<1917:AARMMI>2.0.CO;2
- 637 Wu X, Deng L, Song X, et al (2007) Impact of a modified convective scheme on the
 638 Madden-Julian Oscillation and El Niño - Southern Oscillation in a coupled climate
 639 model. *Geophys Res Lett* 34:. <https://doi.org/10.1029/2007GL030637>
- 640 Yanai M, Esbensen S, Chu J-H (1973) Determination of Bulk Properties of Tropical
 641 Cloud Clusters from Large-Scale Heat and Moisture Budgets. *J Atmos Sci* 30:611–
 642 627
- 643 Zhang C (2005) Madden-Julian Oscillation. *Rev Geophys* 43:RG2003.
 644 <https://doi.org/10.1029/2004RG000158>
- 645 Zhang GJ, Mu M (2005) Effects of modifications to the Zhang-McFarlane convection
 646 parameterization on the simulation of the tropical precipitation in the National

647 Center for Atmospheric Research Community Climate Model, version 3. J
648 Geophys Res D Atmos 110:1–12. <https://doi.org/10.1029/2004JD005617>
649 Zhang GJ, Song X (2009) Interaction of deep and shallow convection is key to Madden-
650 Julian Oscillation simulation. Geophys Res Lett 36:L09708.
651 <https://doi.org/10.1029/2009GL037340>
652
653

654 **Figure Captions**

655

656 **Fig. 1 a–c** Wavenumber–frequency spectra of 850-hPa equatorial zonal winds over 10°
 657 S– 10° N; **d–f** Lag–longitude diagrams of intraseasonal precipitation (shaded area) and
 658 10-m zonal winds (contour) correlated with precipitation averaged over 10° S– 5° N, 75°
 659 E– 100° E. The contour interval is 0.1.

660

661 **Fig. 2** Vertical profiles of intraseasonal anomalies (i.e., with 20-to-100-day band-pass
 662 filtering) in **a–c** moisture convergence (10^{-6} g kg $^{-1}$ s $^{-1}$); **d–f** the apparent heat source (Q_1 ;
 663 K day $^{-1}$); **g–i** the apparent moisture sink (Q_2 ; K day $^{-1}$); and **j–l** moist static energy (10^3 J
 664 kg $^{-1}$ s $^{-1}$), with respect to Madden–Julian Oscillation phases averaged over 10° S, 120° –
 665 150° E. The variables are based on observational data from the ERA-Interim reanalysis,
 666 the Nordeng scheme (E5SIT-Nord) simulation, and the Tiedtke scheme (E5SIT-Tied)
 667 simulation.

668

669 **Fig. 3** Vertical profiles of the unfiltered composite field of the **a–c** apparent heat source
 670 (Q_1 ; K day $^{-1}$) and **d–f** apparent moisture sink (Q_2 ; K day $^{-1}$) plotted with respect to
 671 Madden–Julian Oscillation phases averaged over 10° S, 120 – 150° E. The data are from
 672 the ERA-Interim reanalysis, Nordeng scheme (E5SIT-Nord) simulation, and Tiedtke
 673 scheme (E5SIT-Tied) simulation.

674

675 **Fig. 4** Vertical profiles of apparent heat source (Q_1 ; K day $^{-1}$; red lines) and apparent
 676 moisture sink (Q_2 ; K day $^{-1}$; blue lines) with respect to Madden–Julian Oscillation phases

677 averaged over 10° S and 120° – 150° E for **a–c** phase 1 and **d–f** phase 2. The data are from
 678 the ERA-Interim reanalysis, Nordeng scheme (E5SIT-Nord) simulation, and Tiedtke
 679 scheme (E5SIT-Tied) simulation.

680

681 **Fig. 5** Structure of simulated Madden–Julian Oscillation (MJO) during **a–c** phase 1 and
 682 **d–e** phase 2. The longitude–height cross-sections (averaged over 10° S–EQ) of the MJO-
 683 scaled wind circulation (vector, u : ms^{-1} , ω : $10^{-2} \text{ Pa s}^{-1}$), Q_1 (shaded area; K day^{-1}),
 684 and the horizontal moisture convergence (green contour; $10^{-6} \text{ g kg}^{-1} \text{ s}^{-1}$) in the **a, d** ERA-
 685 Interim reanalysis; **b, e** Nordeng scheme (E5SIT-Nord) simulation, and **c, f** Tiedtke
 686 scheme (E5SIT-Tied) simulation. The contour interval of the moisture convergence is 8
 687 $\times 10^{-6} \text{ g kg}^{-1} \text{ s}^{-1}$. The solid line is positive. Precipitation (shaded area; mm day^{-1}) and sea
 688 level pressure (contour; hPa). The contour interval is 30 hPa. The dashed line is negative.

689

690 **Fig. 6** Regressed structure of circulation patterns, the apparent moisture sink (Q_2), and
 691 moist static energy (MSE) on intraseasonal convective time scale (shown in Fig.S5) in
 692 the **a** ERA-Interim reanalysis, **b** Nordeng scheme (E5SIT-Nord) simulation, and **c**
 693 Tiedtke scheme (E5SIT-Tied) simulation. The MSE ($\text{J kg}^{-1} \text{ s}^{-1}$) is shown in the shaded
 694 area, Q_2 (K day^{-1}) is shown in blue contours, and the circulation winds (ms^{-1}) are shown
 695 as vectors. The left panel shows the horizontal maps of 850-hPa fields, and the right panel
 696 shows the height–longitude cross-sections averaged over 10° S. The blue contour intervals
 697 in the left and right panels are 0.2 and 0.1, respectively.

698

699 **Fig. 7** Vertical profiles of Q_2 (K day^{-1}) composited from categories of rainfall intensity
 700 (mm day^{-1}) over the tropical oceanic regions covering 10° S– 5° N, 80° – 160° E simulated

701 by the **a** Nordeng scheme (E5SIT-Nord) and **b** Tiedtke scheme (E5SIT-Tied); **c** shows
702 the differences between the two simulations. Only the ocean grid is calculated.

703

704 **Fig. 8** Distribution of occurrence of daily rainfall with respect to rainfall intensity and sea
705 surface temperature (SST). The categories were ranked into bins over the tropical oceanic
706 regions covering 10° S–5° N, 80°–160° E simulated by the **a** Nordeng (E5SIT-Nord)
707 scheme and **b** Tiedtke scheme (E5SIT-Tied); **c** shows the differences between the two
708 simulations. Only the ocean grid is calculated.

709

710 **Fig. 9** Differences in circulation patterns and sea level pressure between the Nordeng
711 scheme (E5SIT-Nord) and Tiedtke scheme (E5SIT-Tied) simulations in the form of
712 height–longitude cross-sections over the equator and horizontal maps on **a** day 1 and **b**
713 day 2 after model initiation. The upper panel shows MSE (shaded area; $\text{J kg}^{-1} \text{s}^{-1}$), Q_2
714 (Contours; K day^{-1} , interval is -5,-1,1,5), and circulations (u , m/s ; ω , 10^{-2} Pa/s , with
715 omissions for velocities under 3). The lower panel shows the sea level pressure (shaded
716 area; hPa), and the circulations (m/s for both u and v , with omissions for circulation under
717 0.8 m/s).

718

719 **Fig. 10** Schematic of convection–circulation coupling in the Madden–Julian Oscillation
720 based on the analysis of the Nordeng and Tiedtke scheme simulations during MJO
721 development (over phases 1 and 2). Convection is represented as clouds; convection-
722 induced subsidence and horizontal wind fields are shown as black arrows and color
723 arrows, respectively.

724

725 **Supplementary Figure Captions**

726

727 **Fig. S1** Mean states of **a** 850-hPa zonal winds (m/s) and **b** precipitation (mm/day) in
728 winter (November–April). The black contours are the sea surface temperature ($^{\circ}\text{C}$). From
729 top to bottom, the data are from the ERA-Interim reanalysis, Nordeng scheme (E5SIT-
730 Nord) simulation, and Tiedtke scheme (E5SIT-Tied) simulation.

731

732 **Fig. S2** Maps of ratio of intraseasonal rainfall variability (subjected to 20-to-100-day
733 band-pass filtering) to total rainfall variability (shaded area). Intraseasonal rainfall
734 variability (contours; subjected to 20-to-100-day band-pass filtering). From top to bottom,
735 the daily rainfall data are from the **a** Global Precipitation Climatology Project, **b** Nordeng
736 scheme (E5SIT-Nord) simulation, and **c** Tiedtke scheme (E5SIT-Tied) simulation.

737

738 **Fig. S3 a–c** Mean moisture at 700-hPa (g/kg); **d** Moist bias between Nordeng scheme
739 (E5SIT-Nord) simulation, Tiedtke scheme (E5SIT-Tied) simulation, and ERA-Interim
740 reanalysis over the tropical Indian Ocean and Maritime Continent (20°S – 20°N , 90° –
741 135°E); **e** Pattern correlation coefficient of moisture between the two simulations and the
742 ERA-Interim reanalysis from 1000 to 200 hPa.

743

744 **Fig. S4** Model-simulated column-integrated MSE budget terms ($\text{J kg}^{-1} \text{s}^{-1}$) during phases
745 1 and 2 of the Madden–Julian Oscillation. Data from the observations, Nordeng scheme
746 simulation, and Tiedtke scheme simulation are shown in black, red, and blue, respectively.
747 The averaged domain is 10°S -EQ, 120° – 150°E .

748

749 **Fig. S5 Normalized** time scale data of intraseasonal convective time scale from the ERA-
750 Interim reanalysis (green line), Nordeng scheme (E5SIT-Nord) simulation (orange line),
751 and Tiedtke scheme (E5SIT-Tied) simulation (blue line), averaged over 10° S– 10° N, 90
752 $^{\circ}$ – 150° E.

753

754 **Fig. S6.** Latitude–height cross-sections of the regressed structure to intraseasonal
755 convective time scale (shown in Fig. S5) in the **a** ERA-Interim reanalysis, **b** Nordeng
756 scheme (E5SIT-Nord) simulation, and **c** Tiedtke scheme (E5SIT-Tied) simulation. The
757 shaded area, blue contours, and vectors represent the MSE ($\text{J kg}^{-1} \text{s}^{-1}$), apparent moisture
758 sink (Q_2 ; K day^{-1} ; contour is 0.1), and circulation winds (ms^{-1}), respectively. Height–
759 latitude cross-sections averaged over 120° – 150° E.

760

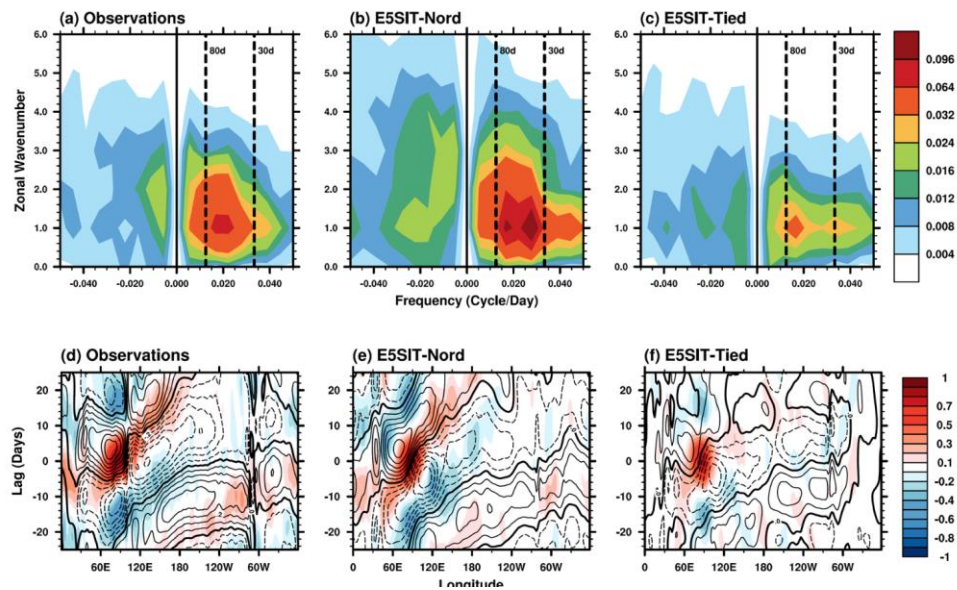


Fig. 2 **a–c** Wavenumber–frequency spectra of 850-hPa equatorial zonal winds over 10° S– 10° N; **d–f** Lag–longitude diagrams of intraseasonal precipitation (shaded area) and 10-m zonal winds (contour) correlated with precipitation averaged over 10° S– 5° N, 75° E– 100° E. The contour interval is 0.1.

761

762

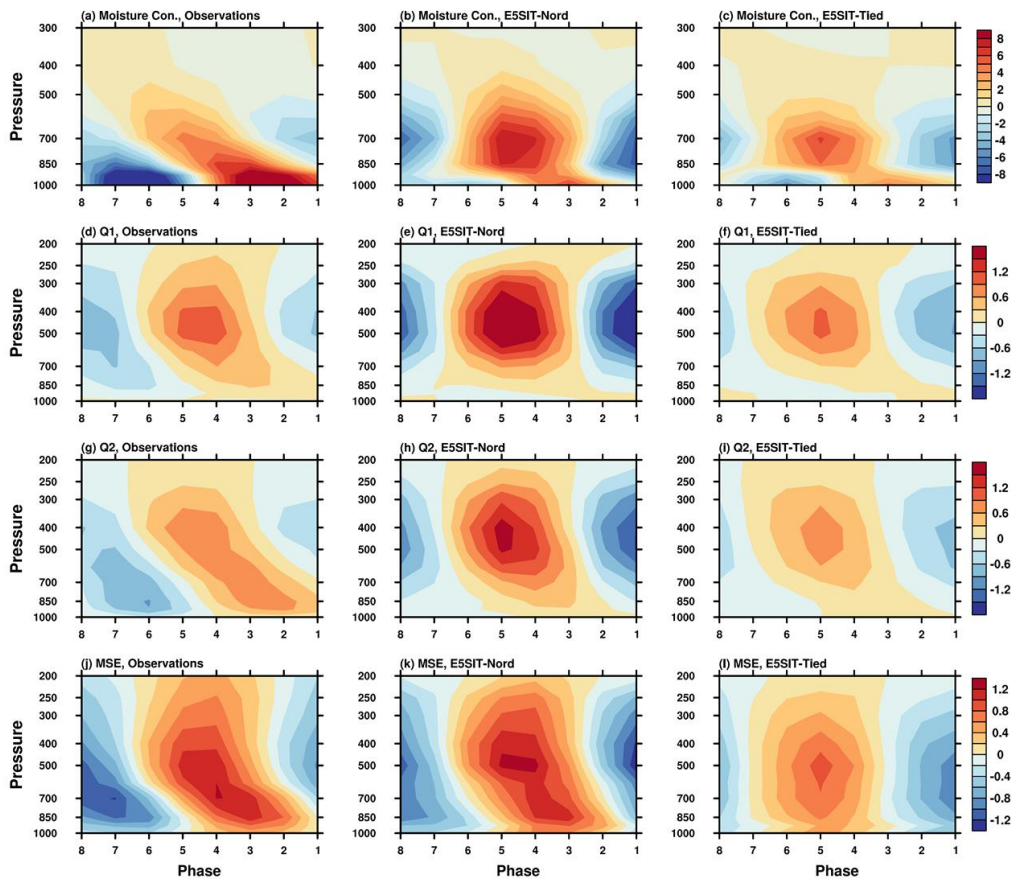
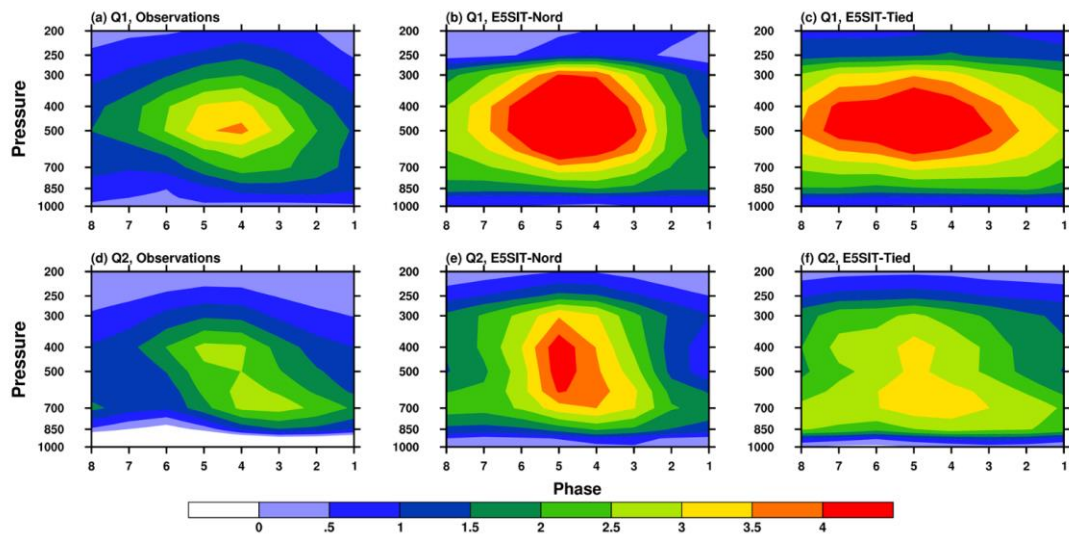


Fig. 2 Vertical profiles of intraseasonal anomalies (i.e., with 20-to-100-day band-pass filtering) in **a–c** moisture convergence ($10^{-6} \text{ g kg}^{-1} \text{ s}^{-1}$); **d–f** the apparent heat source (Q_1 ; K day^{-1}); **g–i** the apparent moisture sink (Q_2 ; K day^{-1}); and **j–l** moist static energy ($10^3 \text{ J kg}^{-1} \text{ s}^{-1}$), with respect to Madden–Julian Oscillation phases averaged over 10° S , $120^\circ\text{--}150^\circ \text{ E}$. The variables are based on observational data from the ERA-Interim reanalysis, the Nordeng scheme (E5SIT-Nord) simulation, and the Tiedtke scheme (E5SIT-Tied) simulation.

763

764



765 **Fig. 3** Vertical profiles of the unfiltered composite field of the **a–c** apparent heat source
 766 (Q_1 ; K day^{-1}) and **d–f** apparent moisture sink (Q_2 ; K day^{-1}) plotted with respect to
 767 Madden–Julian Oscillation phases averaged over 10° S , $120\text{--}150^\circ \text{ E}$. The data are from
 768 the ERA-Interim reanalysis, Nordeng scheme (E5SIT-Nord) simulation, and Tiedtke
 769 scheme (E5SIT-Tied) simulation.

770 .

771

772

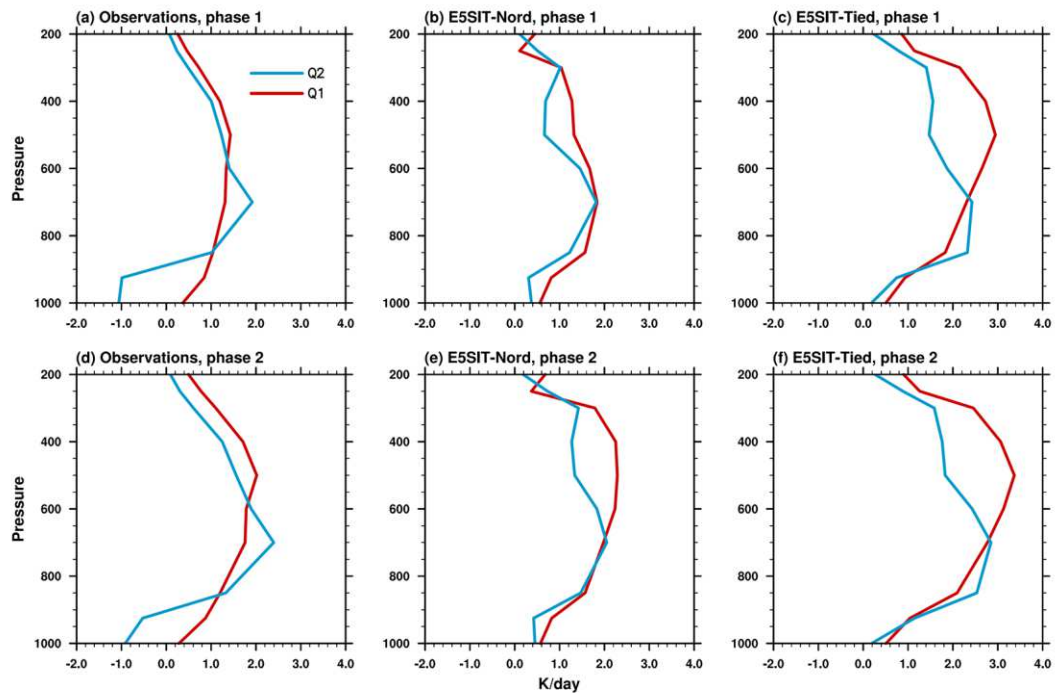


Fig. 4 Vertical profiles of apparent heat source (Q_1 ; K day^{-1} ; red lines) and apparent moisture sink (Q_2 ; K day^{-1} ; blue lines) with respect to Madden–Julian Oscillation phases averaged over 10° S and $120^\circ\text{--}150^\circ \text{ E}$ for **a–c** phase 1 and **d–f** phase 2. The data are from the ERA-Interim reanalysis, Nordeng scheme (E5SIT-Nord) simulation, and Tiedtke scheme (E5SIT-Tied) simulation.

773

•

774

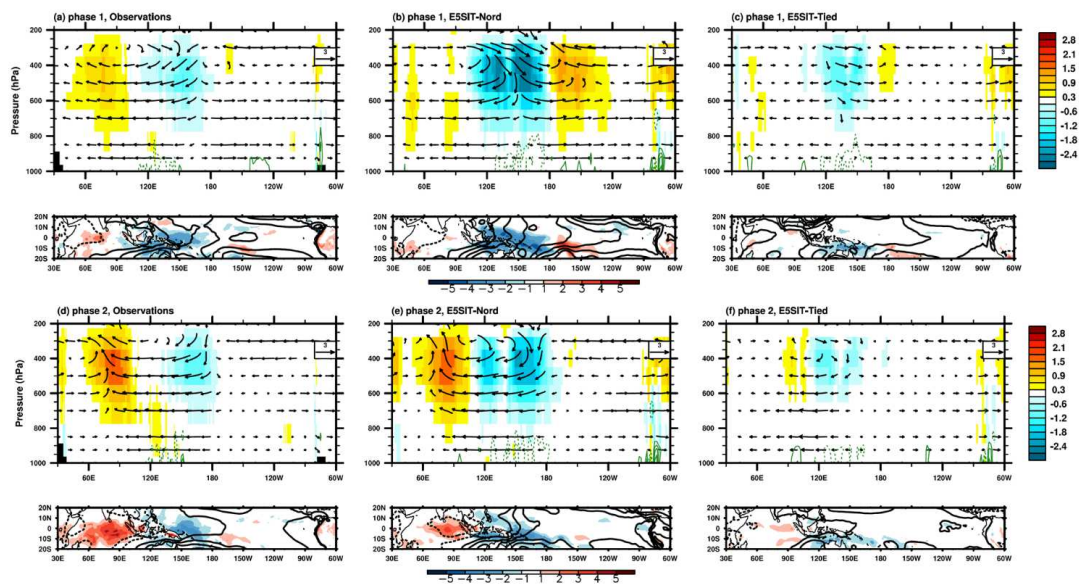


Fig. 5 Structure of simulated Madden–Julian Oscillation (MJO) during **a–c** phase 1 and **d–e** phase 2. The longitude–height cross-sections (averaged over 10 °S–EQ) of the MJO-scaled wind circulation (vector, u : ms^{-1} , ω : $10^{-2} \text{ Pa s}^{-1}$), Q_I (shaded area; K day^{-1}), and the horizontal moisture convergence (green contour; $10^{-6} \text{ g kg}^{-1} \text{ s}^{-1}$) in the **a, d** ERA-Interim reanalysis; **b, e** Nordeng scheme (E5SIT-Nord) simulation, and **c, f** Tiedtke scheme (E5SIT-Tied) simulation. The contour interval of the moisture convergence is $8 \times 10^{-6} \text{ g kg}^{-1} \text{ s}^{-1}$. The solid line is positive. Precipitation (shaded area; mm day^{-1}) and sea level pressure (contour; hPa). The contour interval is 30 hPa. The dashed line is negative.

775

776

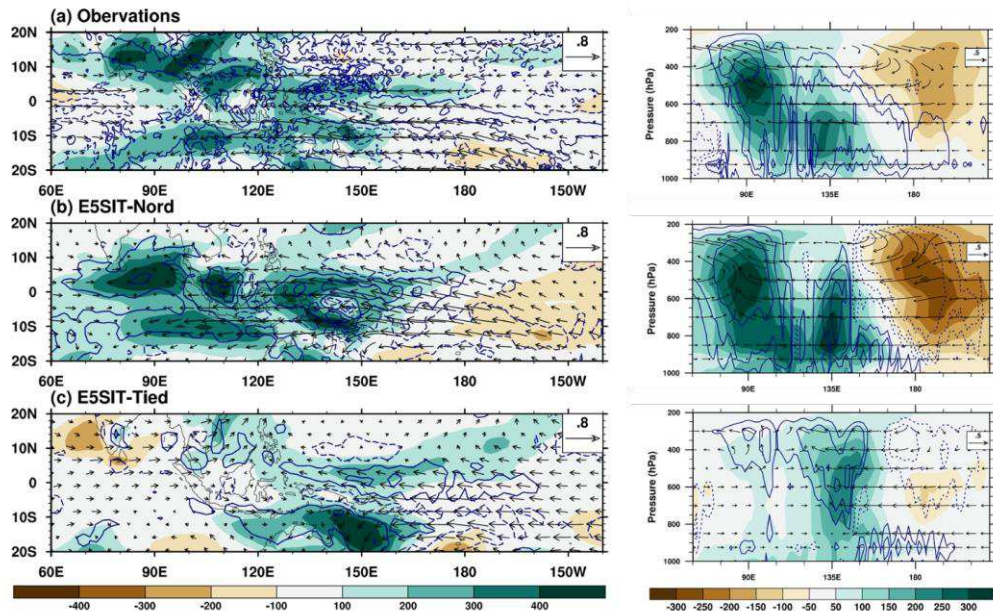
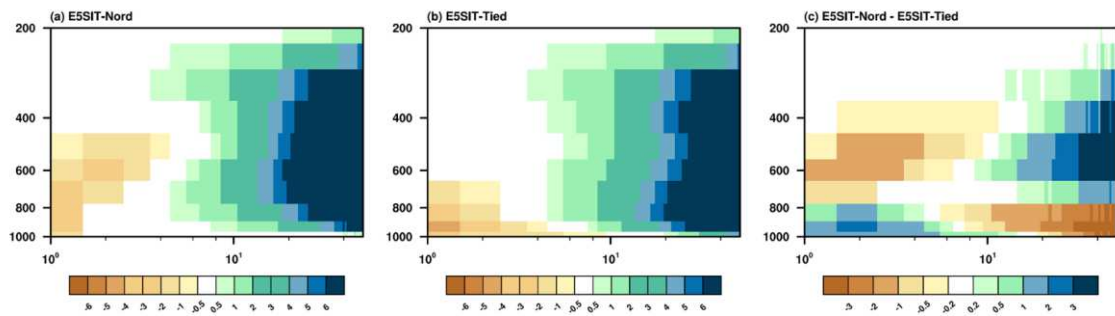


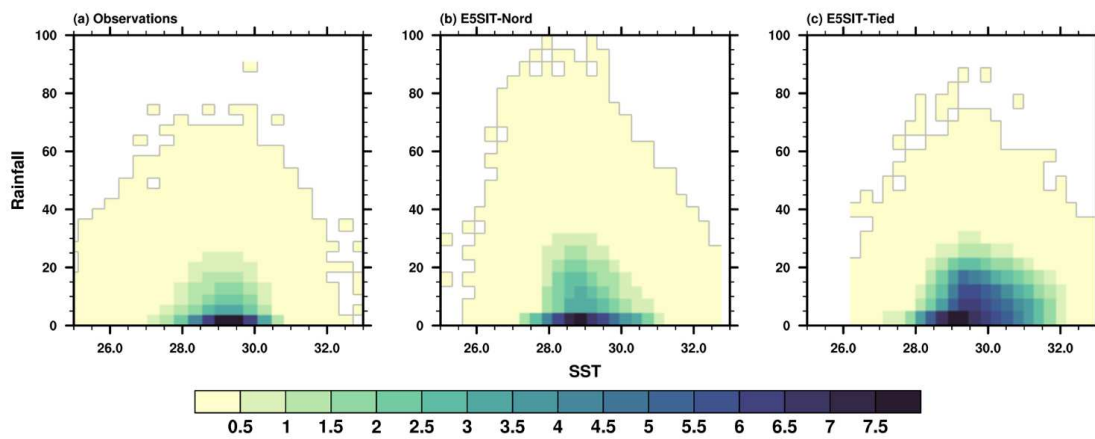
Fig. 6 Regressed structure of circulation patterns, the apparent moisture sink (Q_2), and moist static energy (MSE) on intraseasonal convective time scale (shown in Fig.S5) in the **a** ERA-Interim reanalysis, **b** Nordeng scheme (E5SIT-Nord) simulation, and **c** Tiedtke scheme (E5SIT-Tied) simulation. The MSE ($\text{J kg}^{-1} \text{s}^{-1}$) is shown in the shaded area, Q_2 (K day^{-1}) is shown in blue contours, and the circulation winds (ms^{-1}) are shown as vectors. The left panel shows the horizontal maps of 850-hPa fields, and the right panel shows the height-longitude cross-sections averaged over 10°S . The blue contour intervals in the left and right panels are 0.2 and 0.1, respectively.



778

779 **Fig. 7** Vertical profiles of Q_2 (K day^{-1}) composited from categories of rainfall intensity
 780 (mm day^{-1}) over the tropical oceanic regions covering 10°S – 5°N , 80° – 160°E simulated
 781 by the **a** Nordeng scheme (E5SIT-Nord) and **b** Tiedtke scheme (E5SIT-Tied); **c** shows
 782 the differences between the two simulations. Only the ocean grid is calculated.

783

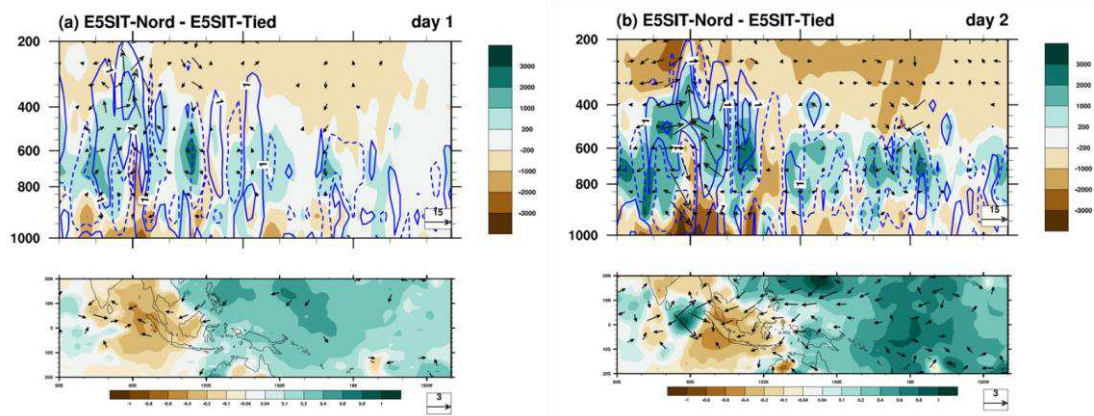


784

785 **Fig. 8** Distribution of occurrence of daily rainfall with respect to rainfall intensity and sea
 786 surface temperature (SST). The categories were ranked into bins over the tropical oceanic
 787 regions covering 10° S– 5° N, 80° – 160° E simulated by the **a** Nordeng (E5SIT-Nord)
 788 scheme and **b** Tiedtke scheme (E5SIT-Tied); **c** shows the differences between the two
 789 simulations. Only the ocean grid is calculated.

790

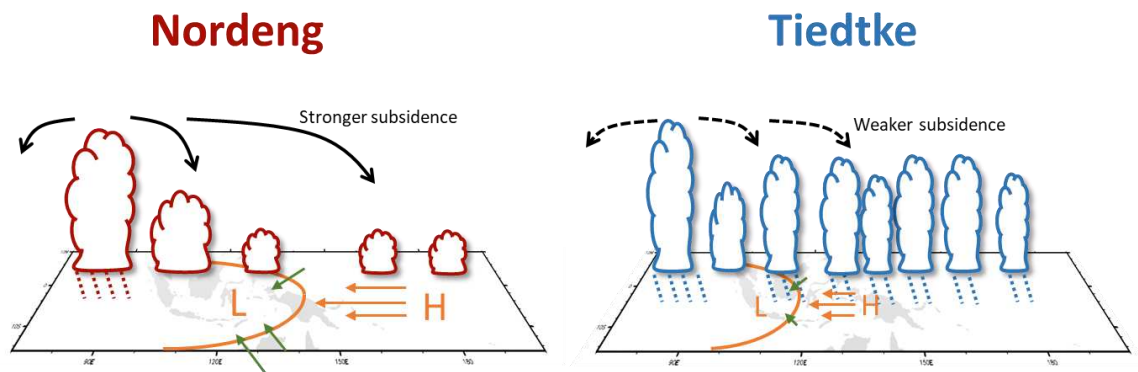
791



792

793 **Fig. 9** Differences in circulation patterns and sea level pressure between the Nordeng
 794 scheme (E5SIT-Nord) and Tiedtke scheme (E5SIT-Tied) simulations in the form of
 795 height–longitude cross-sections over the equator and horizontal maps on **a** day 1 and **b**
 796 day 2 after model initiation. The upper panel shows MSE (shaded area; $\text{J kg}^{-1} \text{s}^{-1}$), Q_2
 797 (Contours; K day^{-1} , interval is -5,-1,1,5), and circulations (u , m/s ; ω , 10^{-2} Pa/s , with
 798 omissions for velocities under 3). The lower panel shows the sea level pressure (shaded
 799 area; hPa), and the circulations (m/s for both u and v , with omissions for circulation under
 800 0.8 m/s).

801



802

803

804 **Fig. 10** Schematic of convection–circulation coupling in the Madden–Julian Oscillation
 805 based on the analysis of the Nordeng and Tiedtke scheme simulations during MJO
 806 development (over phases 1 and 2). Convection is represented as clouds; convection-
 807 induced subsidence and horizontal wind fields are shown as black arrows and color
 808 arrows, respectively.

809

Figures

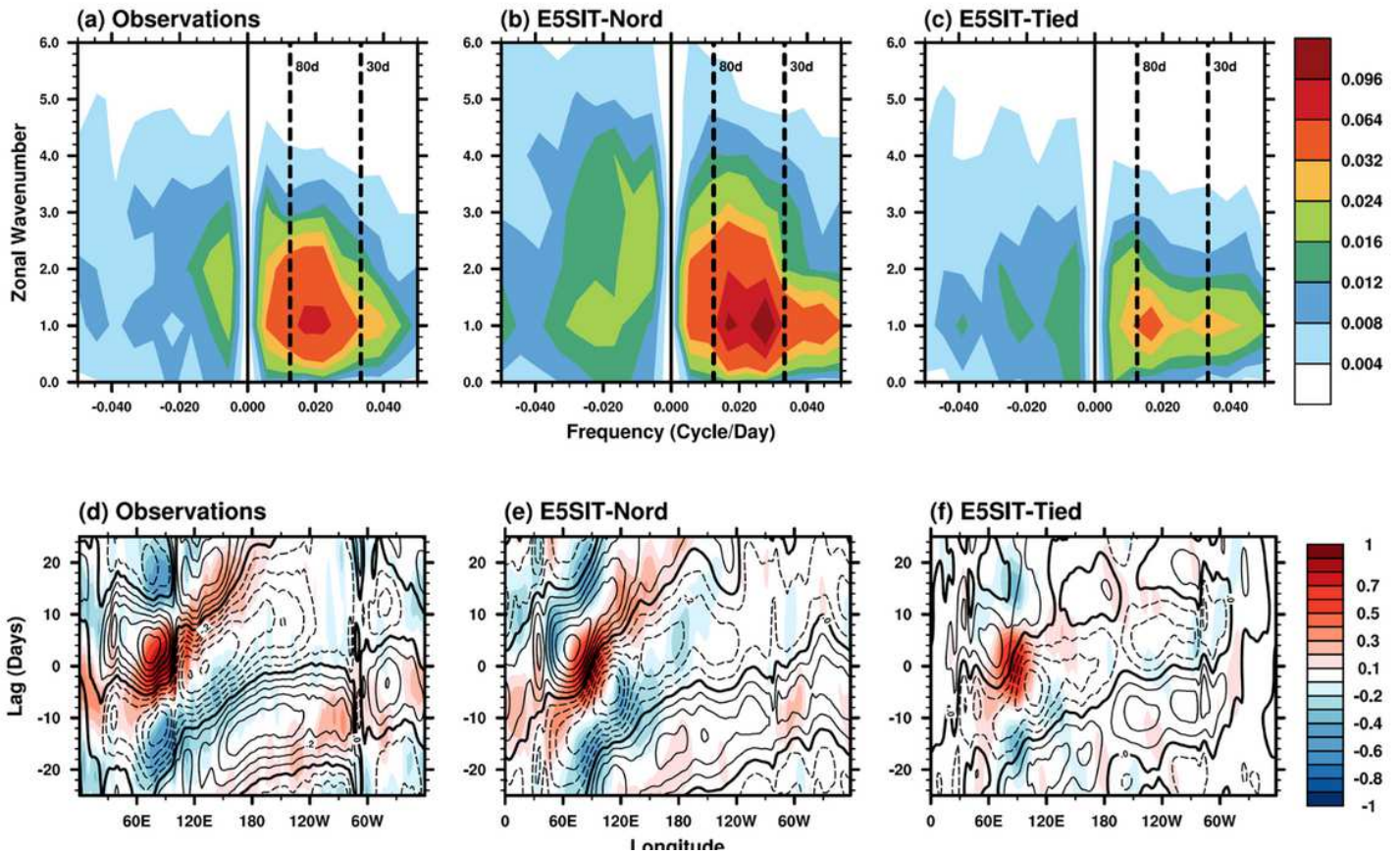


Figure 1

a–c Wavenumber–frequency spectra of 850-hPa equatorial zonal winds over 10° S– 10° N; d–f Lag–longitude diagrams of intraseasonal precipitation (shaded area) and 10-m zonal winds (contour) correlated with precipitation averaged over 10° S– 5° N, 75° E– 100° E. The contour interval is 0.1.

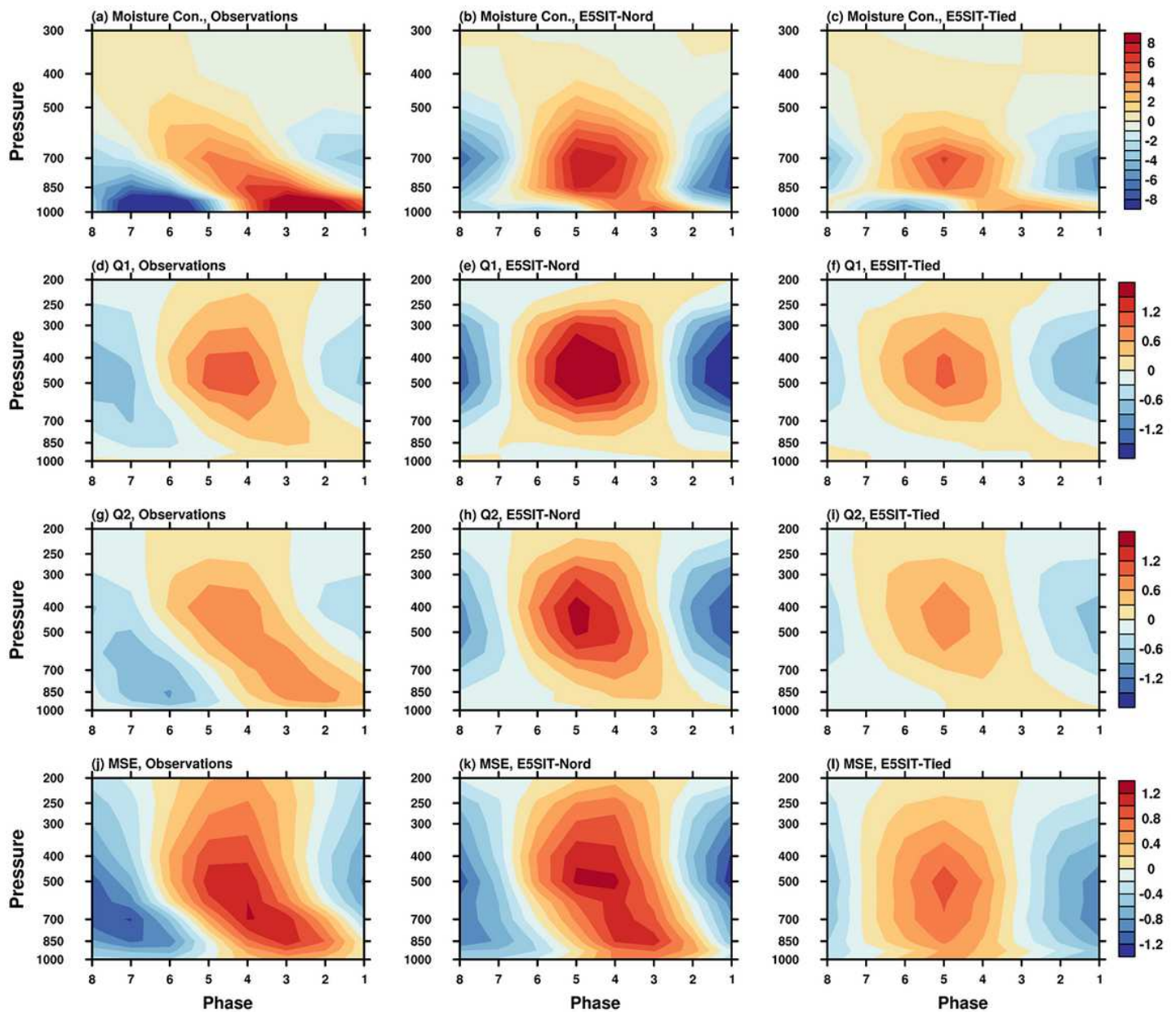


Figure 2

Vertical profiles of intraseasonal anomalies (i.e., with 20-to-100-day band-pass filtering) in a–c moisture convergence ($10^{-6} \text{ g kg}^{-1} \text{ s}^{-1}$); d–f the apparent heat source (Q1; K day^{-1}); g–i the apparent moisture sink (Q2; K day^{-1}); and j–l moist static energy ($10^3 \text{ J kg}^{-1} \text{ s}^{-1}$), with respect to Madden–Julian Oscillation phases averaged over 10° S , $120^\circ\text{--}150^\circ \text{ E}$. The variables are based on observational data from the ERA-Interim reanalysis, the Nordeng scheme (E5SIT-Nord) simulation, and the Tiedtke scheme (E5SIT-Tied) simulation.

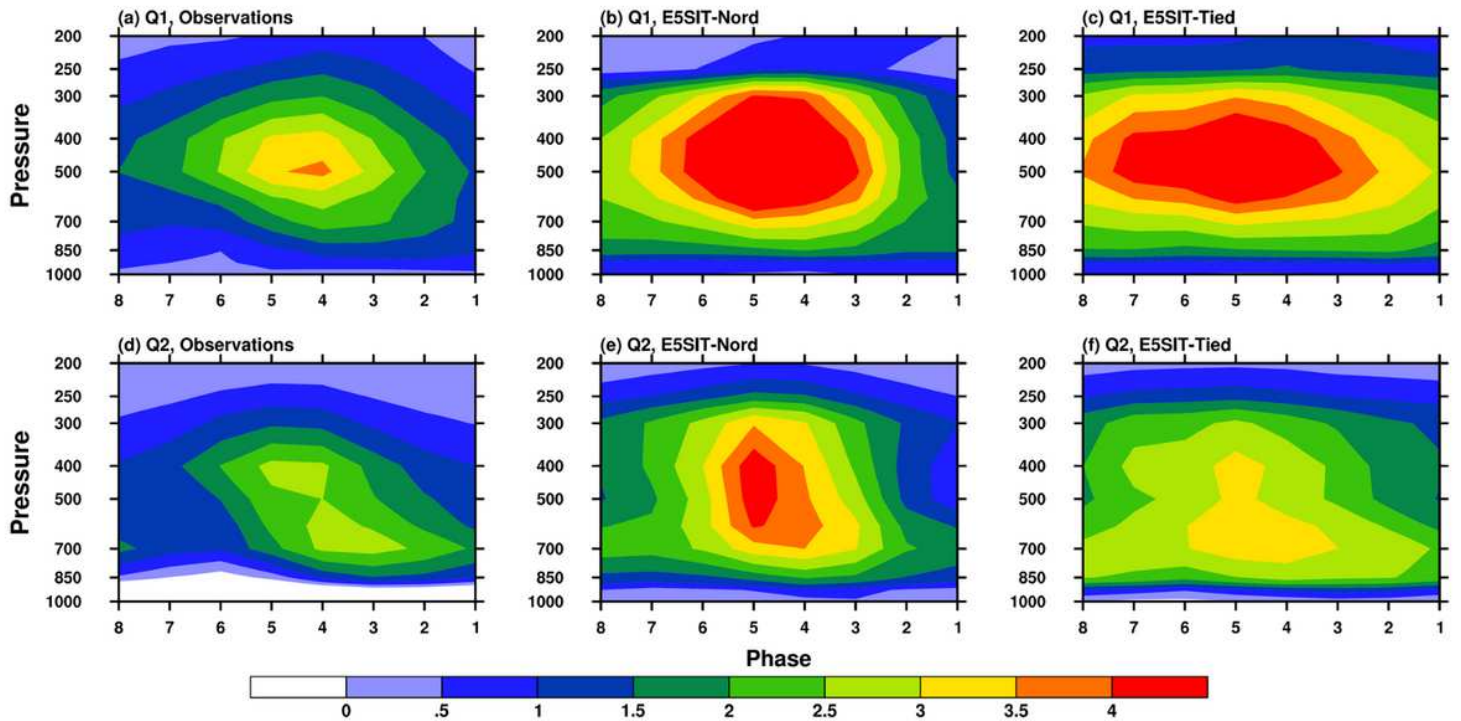


Figure 3

Vertical profiles of the unfiltered composite field of the a–c apparent heat source (Q1; K day⁻¹) and d–f apparent moisture sink (Q2; K day⁻¹) plotted with respect to Madden–Julian Oscillation phases averaged over 10° S, 120–150 °E. The data are from the ERA-Interim reanalysis, Nordeng scheme (E5SIT-Nord) simulation, and Tiedtke scheme (E5SIT-Tied) simulation.

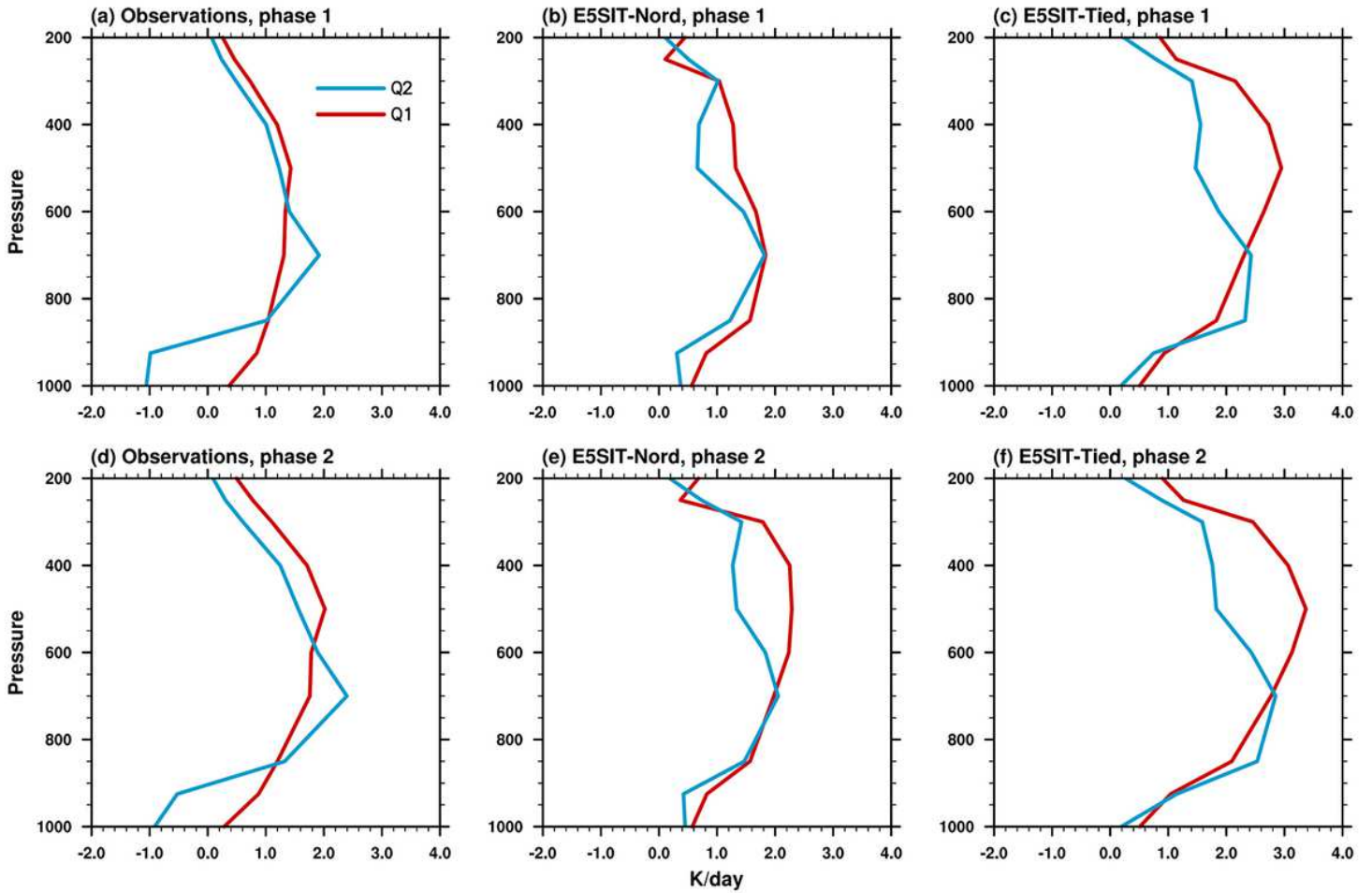


Figure 4

Vertical profiles of apparent heat source (Q1; K day⁻¹; red lines) and apparent moisture sink (Q2; K day⁻¹; blue lines) with respect to Madden–Julian Oscillation phases averaged over 10° S and 120°–150° E for a–c phase 1 and d–f phase 2. The data are from the ERA-Interim reanalysis, Nordeng scheme (E5SIT-Nord) simulation, and Tiedtke scheme (E5SIT-Tied) simulation.

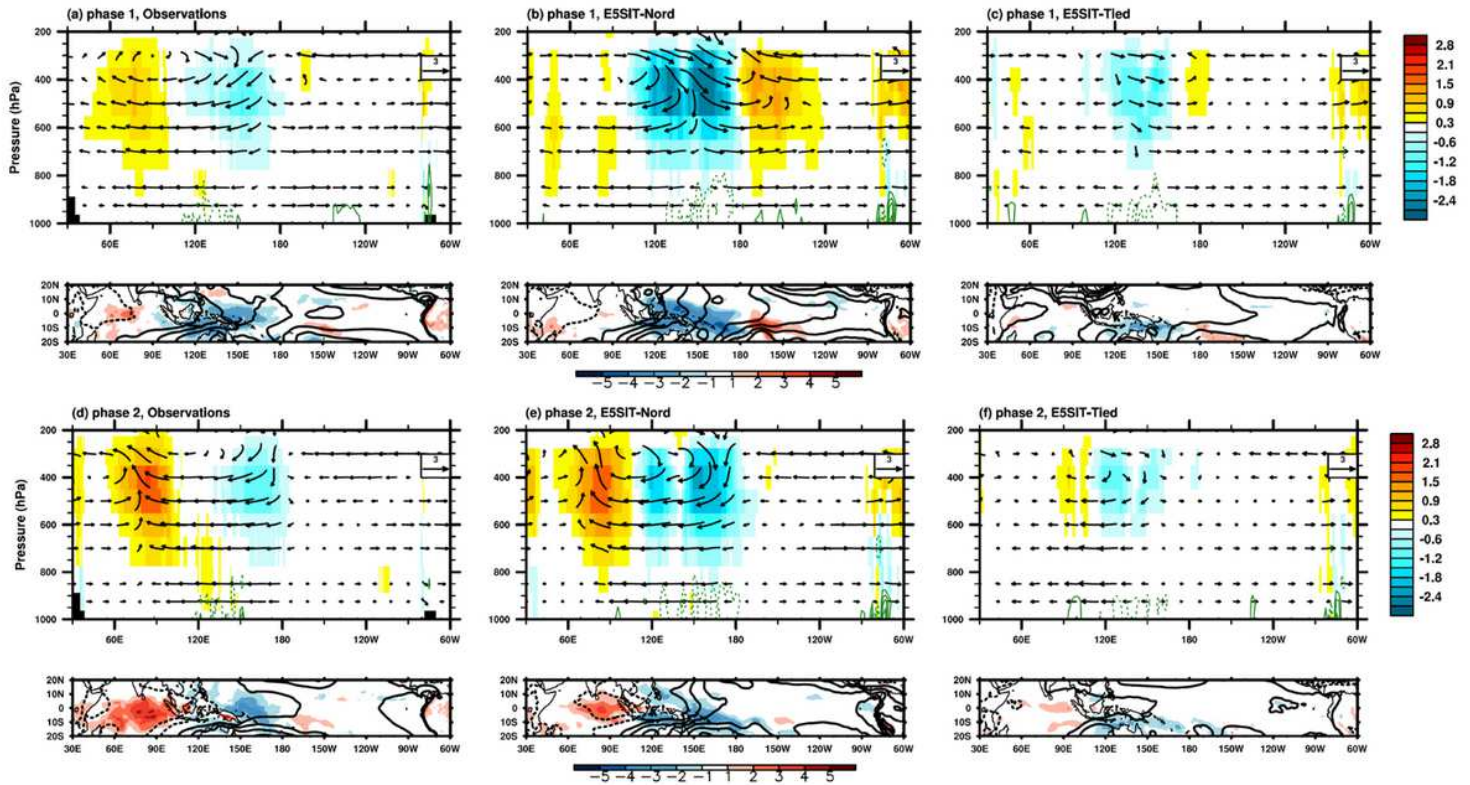


Figure 5

Structure of simulated Madden–Julian Oscillation (MJO) during a–c phase 1 and d–e phase 2. The longitude–height cross-sections (averaged over 10 °S–EQ) of the MJO-scaled wind circulation (vector, u : ms^{-1} , ω : $10^{-2} \text{ Pa s}^{-1}$), $Q1$ (shaded area; K day^{-1}), and the horizontal moisture convergence (green contour; $10^{-6} \text{ g kg}^{-1} \text{ s}^{-1}$) in the a, d ERA-Interim reanalysis; b, e Nordeng scheme (E5SIT-Nord) simulation, and c, f Tiedtke scheme (E5SIT-Tied) simulation. The contour interval of the moisture convergence is $8 \times 10^{-6} \text{ g kg}^{-1} \text{ s}^{-1}$. The solid line is positive. Precipitation (shaded area; mm day^{-1}) and sea level pressure (contour; hPa). The contour interval is 30 hPa. The dashed line is negative. Note: The designations employed and the presentation of the material on this map do not imply the expression of any opinion whatsoever on the part of Research Square concerning the legal status of any country, territory, city or area or of its authorities, or concerning the delimitation of its frontiers or boundaries. This map has been provided by the authors.

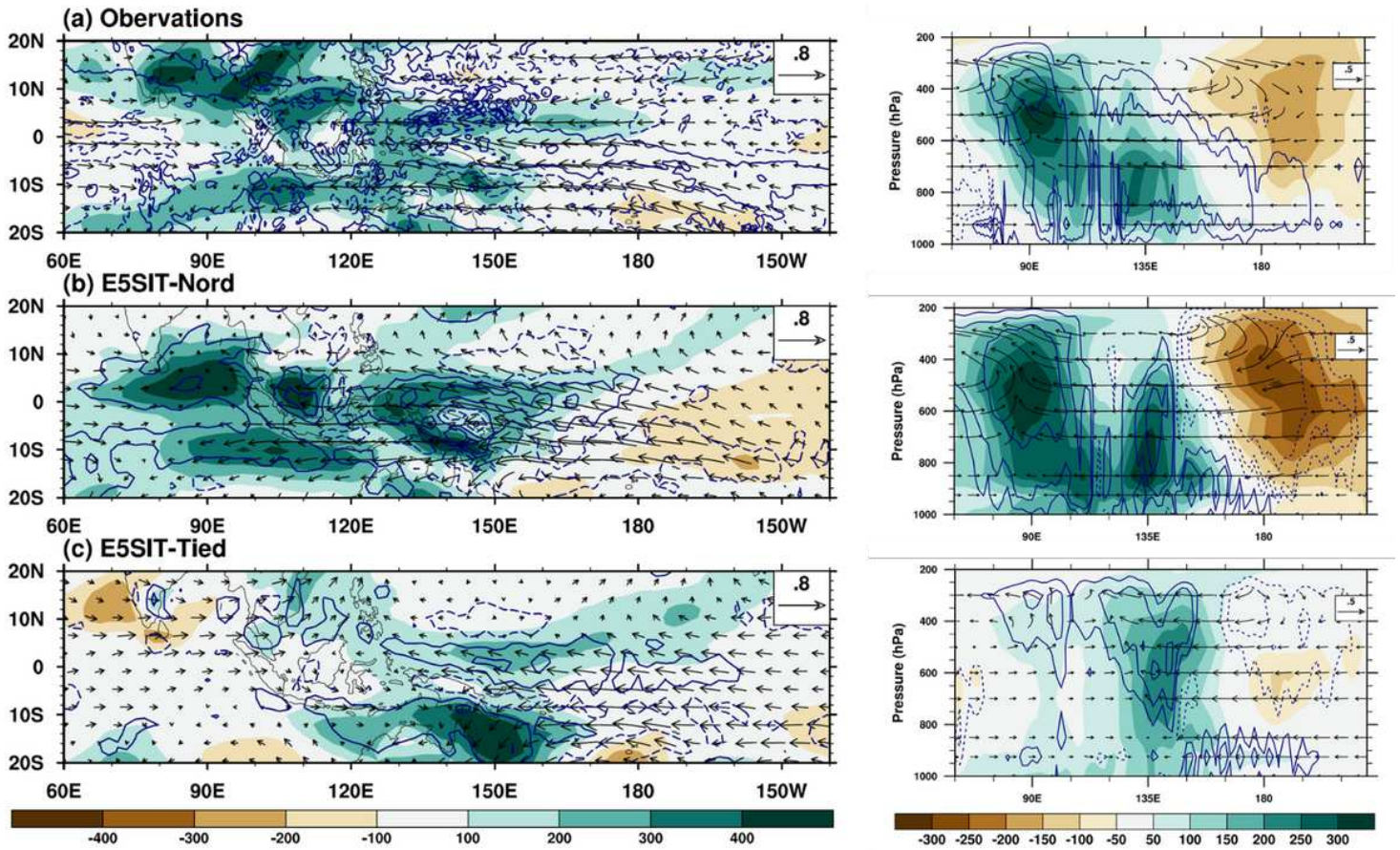


Figure 6

Regressed structure of circulation patterns, the apparent moisture sink (Q2), and moist static energy (MSE) on intraseasonal convective time scale (shown in Fig.S5) in the a ERA-Interim reanalysis, b Nordeng scheme (E5SIT-Nord) simulation, and c Tiedtke scheme (E5SIT-Tied) simulation. The MSE ($\text{J kg}^{-1} \text{s}^{-1}$) is shown in the shaded area, Q2 (K day^{-1}) is shown in blue contours, and the circulation winds (ms^{-1}) are shown as vectors. The left panel shows the horizontal maps of 850-hPa fields, and the right panel shows the height-longitude cross-sections averaged over 10°S . The blue contour intervals in the left and right panels are 0.2 and 0.1, respectively. Note: The designations employed and the presentation of the material on this map do not imply the expression of any opinion whatsoever on the part of Research Square concerning the legal status of any country, territory, city or area or of its authorities, or concerning the delimitation of its frontiers or boundaries. This map has been provided by the authors.

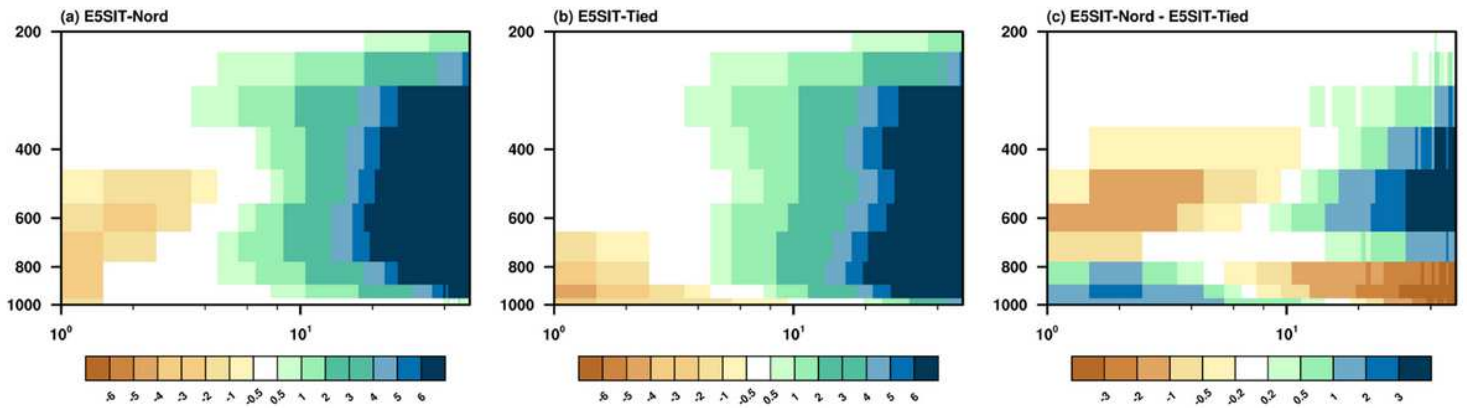


Figure 7

Vertical profiles of Q2 (K day^{-1}) composited from categories of rainfall intensity (mm day^{-1}) over the tropical oceanic regions covering $10^\circ \text{ S} - 5^\circ \text{ N}$, $80^\circ - 160^\circ \text{ E}$ simulated by the a Nordeng scheme (E5SIT-Nord) and b Tiedtke scheme (E5SIT-Tied); c shows the differences between the two simulations. Only the ocean grid is calculated. Note: The designations employed and the presentation of the material on this map do not imply the expression of any opinion whatsoever on the part of Research Square concerning the legal status of any country, territory, city or area or of its authorities, or concerning the delimitation of its frontiers or boundaries. This map has been provided by the authors.

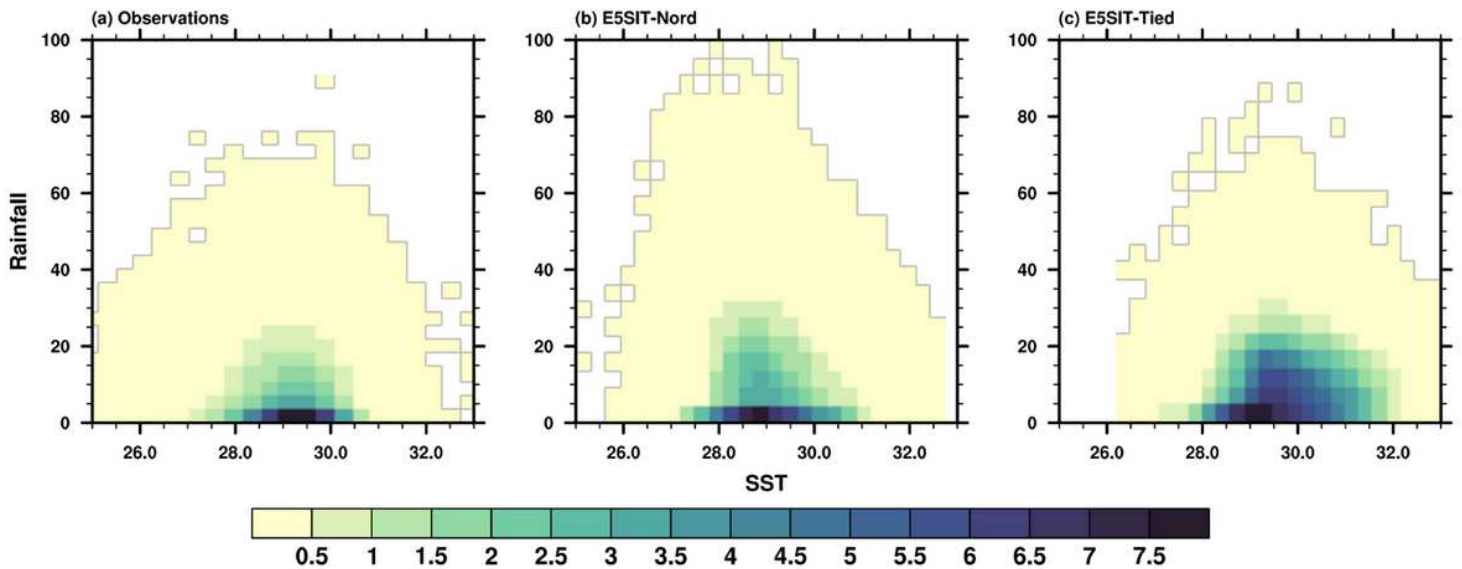


Figure 8

Distribution of occurrence of daily rainfall with respect to rainfall intensity and sea surface temperature (SST). The categories were ranked into bins over the tropical oceanic regions covering $10^\circ \text{ S} - 5^\circ \text{ N}$, $80^\circ - 160^\circ \text{ E}$ simulated by the a Nordeng (E5SIT-Nord) scheme and b Tiedtke scheme (E5SIT-Tied); c shows the differences between the two simulations. Only the ocean grid is calculated.

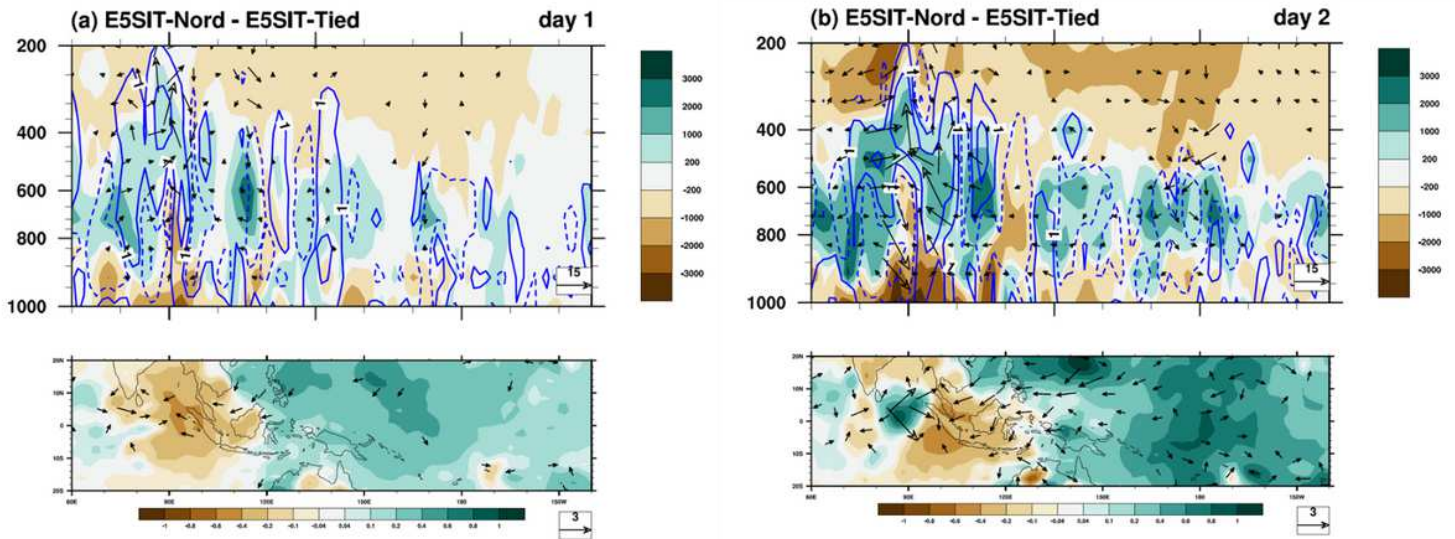


Figure 9

Differences in circulation patterns and sea level pressure between the Nordeng scheme (E5SIT-Nord) and Tiedtke scheme (E5SIT-Tied) simulations in the form of height–longitude cross-sections over the equator and horizontal maps on a day 1 and b day 2 after model initiation. The upper panel shows MSE (shaded area; $\text{J kg}^{-1} \text{ s}^{-1}$), Q2 (Contours; K day^{-1} , interval is -5,-1,1,5), and circulations (u , m/s ; ω , 10^{-2} Pa/s , with omissions for velocities under 3). The lower panel shows the sea level pressure (shaded area; hPa), and the circulations (m/s for both u and v , with omissions for circulation under 0.8 m/s). Note: The designations employed and the presentation of the material on this map do not imply the expression of any opinion whatsoever on the part of Research Square concerning the legal status of any country, territory, city or area or of its authorities, or concerning the delimitation of its frontiers or boundaries. This map has been provided by the authors.

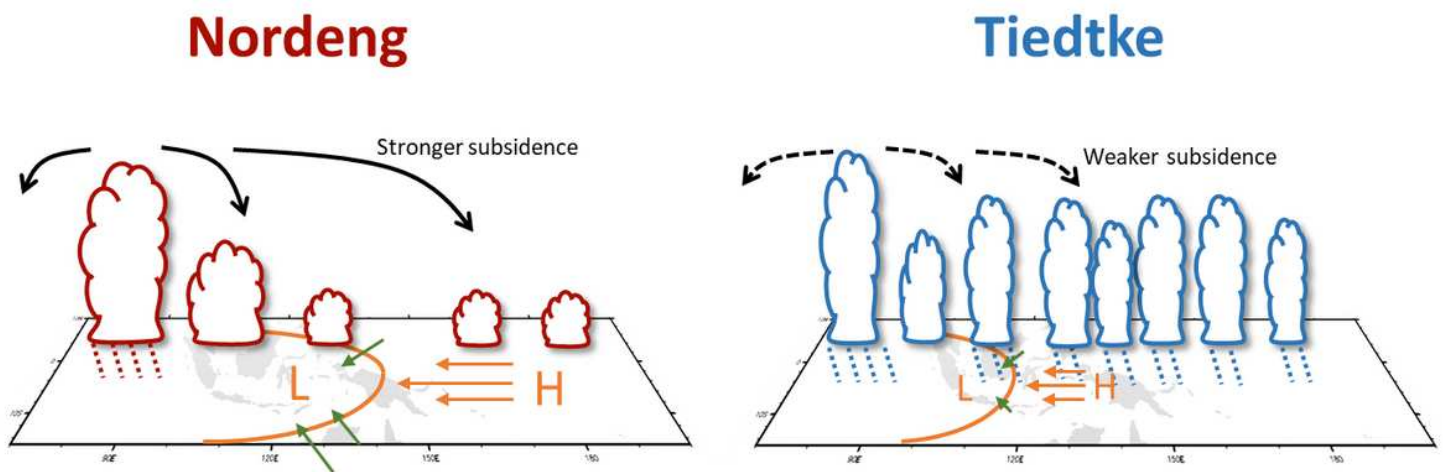


Figure 10

Schematic of convection–circulation coupling in the Madden–Julian Oscillation based on the analysis of the Nordeng and Tiedtke scheme simulations during MJO development (over phases 1 and 2).

Convection is represented as clouds; convection-induced subsidence and horizontal wind fields are shown as black arrows and color arrows, respectively.

Supplementary Files

This is a list of supplementary files associated with this preprint. Click to download.

- [CLDYfinalSI.pdf](#)